We are IntechOpen, the world's leading publisher of Open Access books Built by scientists, for scientists

4,800
Open access books available

122,000
International authors and editors

135M
Downloads

Our authors are among the

154
Countries delivered to

TOP 1%
most cited scientists

12.2%
Contributors from top 500 universities

WEB OF SCIENCE™

Selection of our books indexed in the Book Citation Index in Web of Science™ Core Collection (BKCI)

Interested in publishing with us?
Contact book.department@intechopen.com

Numbers displayed above are based on latest data collected.
For more information visit www.intechopen.com

Chapter 8

Piezoelectric-Layered Structures Based on Synthetic Diamond

Boris P. Sorokin, Gennady M. Kvashnin, Arsenii V. Telichko, Sergey I. Burkov and Vladimir D. Blank

Additional information is available at the end of the chapter

http://dx.doi.org/10.5772/62630

Abstract

Results of theoretical, modeling, and experimental investigation of microwave acoustic properties of piezoelectric layered structure "Me1/AlN/Me2/(100) diamond" have been presented within a wide frequency band 0.5–10 GHz. The highest among known material quality parameter $Q \times f \sim 10^{14}$ Hz for the IIa type synthetic diamond at operational frequency ~10 GHz has been found. Conditions of UHF excitation and propagation of the bulk, surface, and Lamb plate acoustic waves have been established and studied experimentally. Frequency dependencies of the impedance and quality factor have been studied to obtain a number of piezoelectric layered structure parameters as electromechanical coupling coefficient, equivalent circuit parameters, etc. Results of 2D finite element modeling of a given piezoelectric layered structure have been compared with the experimental ones obtained for the real high-overtone bulk acoustic resonator. An origin of high-overtone bulk acoustic resonator's spurious resonant peaks has been studied. Results on UHF acoustic attenuation of IIa-type synthetic single crystalline diamond have been presented and discussed in terms of Akhiezer and Landau–Rumer mechanisms of phonon–phonon interaction. Identification and classification of Lamb waves belonging to several branches as well as dispersive curves of phase velocities have been executed. Necessity of introducing a more correct Lamb-mode classification has been recognized.

Keywords: aluminum nitride, synthetic diamond, ultra-high frequency, bulk acoustic wave, Lamb wave, electromechanical coupling, acoustic attenuation

1. Introduction

Known piezoelectric materials such as quartz, lithium niobate, lithium tantalate, langasite, etc. have been widely used as the substrates in a number of acoustoelectronic devices such as resonators, acoustic filters, delay lines, sensors, etc. Such devices can operate on one or several types of acoustic waves, such as conventional bulk (BAW) acoustic waves, surface (SAW) acoustic waves (Rayleigh, Sezawa, Gulyaev-Bleustein, shear-horizontal (*SH*), and Love waves), normal plate waves of Lamb-type, and Stoneley acoustic waves on the interface between two different solids. In the twenty-first century, state-of-art technologies have a clear requirement for passive electronic and acoustoelectronic components operating at high and ultra-high (UHF) frequencies with low insertion losses. Previously, conventional structures and materials could not be applied at UHF due to their high acoustic attenuation. Possible solution is to use piezoelectric layered structures (PLS) based on appropriate single crystalline substrates with low UHF acoustic attenuation. Modern precise technologies of thin-film deposition provide fabrication of submicron piezoelectric layers with excellent parameters. Hexagonal aluminum nitride (AlN) films are used more often than zinc oxide (ZnO) films due to their best dielectric properties and thermal stability. Applying PLS approach, one can extend a set of substrate materials to be used up to non-piezoelectric crystals with outstanding physical properties.

Well-known types of BAW resonators are the conventional piezoelectric resonators more often produced out of crystalline quartz, including the high-frequency resonator as inverse mesa structure, thin-film bulk acoustic resonators (FBAR) [1], and solidly mounted resonators (SMR) [1,2], but they have significantly lower both *Q* factor and operating frequencies compared to high overtone bulk acoustic resonator (HBAR). Such HBARs can be used at high frequencies up to 10 GHz because the elastic energy is mainly concentrated within the substrate material [3]. Usually HBARs are designed as PLS with a specified electrode structure deposed on a crystalline substrate with low UHF acoustic attenuation. In earlier investigated BAW resonators, single crystalline and fused quartz, silicon [4], sapphire [4,5], and yttrium aluminum garnet (YAG) substrates [6] were used. It was proved that diamond single crystal has a low acoustic attenuation at UHF and diamond-based HBARs are known operating at frequencies up to 20 GHz [3].

The choice of HBAR's substrate material is a problem of high importance since it is necessary to take into account an appropriate combination of physical and chemical properties, low acoustic attenuation at UHF, crystalline quality, possibility of precise treatment, etc. It is well known that physical properties of thin films such as the density and elastic constants can considerably differ from the ones measured on the bulk specimens. HBAR can be used as an instrument for determination of material properties of substrates and thin films at microwave frequencies with high accuracy. Additionally, HBAR application gives a unique possibility to measure frequency-sensitive properties, for example, the acoustic attenuation of substrate's material within a wide frequency range of 0.5–10 GHz.

Application of diamond as a substrate material in this chapter is caused by its unique physical and acoustical properties: it is the hardest crystal with highest BAW and SAW velocities (in [111] direction, the phase velocity of BAW longitudinal type v_l = 18860 m/s [7]); it has high

thermal conductivity up to 2200 W/cm·K [8]; high thermal and radiation stabilities [9]; low acoustical losses at UHF [10], and so on. As there are many types of diamond crystals, which vary in terms of boron or nitrogen doping concentration, here we will discuss only dielectric IIa-type synthetic diamond crystals with low impurities concentration: $N < 2$ ppm.

The main objectives of this chapter consist of the theoretical, experimental, and modeling study of acoustic wave propagation, especially Lamb modes, and its dispersive properties in diamond-based piezoelectric layered structures.

2. Acoustic modes propagated in piezoelectric layered structures

2.1. Piezoelectric layered structure as a complex acoustic system: normal bulk, surface and plate acoustic waves

Propagation of the small amplitude acoustic waves in the piezoelectric crystal is described by the equations of motion and electrostatics and, additionally, the equations of state of the piezoelectric medium as [11]:

$$\begin{aligned} \rho_0 \ddot{\tilde{U}}_l &= \tilde{\tau}_{ik,k}, \\ \tilde{D}_{m,m} &= 0, \\ \tilde{\tau}_{ik} &= C^E_{ikpq}\tilde{\eta}_{pq} - e_{nik}\tilde{E}_n, \\ \tilde{D}_n &= e_{nik}\tilde{\eta}_{ik} + \varepsilon^{\eta}_{mn}\tilde{E}_m. \end{aligned} \tag{1}$$

There were introduced the values to be used as follows: ϱ_0 is the crystal density; $\widetilde{U}_i$ is the unit vector of the dynamical elastic displacement; τ_{ik} is the thermodynamical stress tensor; η_{ab} is the strain tensor; E_m and D_m are the vectors of electric field and electric displacement, respectively; C^E_{ikpq}, e_{nik}, and ε^{η}_{mn} are the elastic, piezoelectric, and clamped dielectric constants, respectively. Here and after, the time-dependent variables are marked by "tilde" symbol. The comma after the subscript denotes that the spatial derivatives and coordinate Latin indices vary from 1 to 3. Here and further, the rule of summation over repeated indices is used.

Taking into account the dispersion of the elastic waves, a general form of the Christoffel equation and its components can be written as follows:

$$\begin{aligned} \left(\Gamma_{ik} - \rho_0\omega^2\delta_{ik}\right)\alpha_i = 0; i,k = 1,\ldots,4; \delta_{44} = 0; \\ \Gamma_{ik} = C^E_{ijkm}k_j k_m; \\ \Gamma_{4j} = \Gamma_{j4} = e_{ijk}k_i k_k; \Gamma_{44} = -\varepsilon^{\eta}_{nm}k_n k_m; \end{aligned} \tag{2}$$

where $\vec{k} = (\omega/v)\vec{n}$ is the wave vector and $\vec{n}$ is the unit vector of the wave normal; α_i are the eigenvectors (components of wave elastic displacement); α_4 is the amplitude of the wave of

quasi-static electrical potential; ω is the circular frequency, and υ is the phase velocity. Solution of Christoffel equation as a standard problem of the eigenvalues and eigenvectors brings determining the characteristics of the bulk acoustic wave in a piezoelectric crystal.

The propagation of elastic waves in the multilayer piezoelectric structure should be written introducing additionally the boundary conditions depending on the number m of layer:

$$\begin{aligned}
&\tau_{3j}^{(1)} = 0\big|_{x_3=h_1}, \quad D_3^{(1)} = D^{(vac)}\Big|_{x_3=h_1};\\
&\tau_{3j}^{(1)} = \tau_{3j}^{(2)}\Big|_{x_3=h_2}, \quad D_3^{(1)} = D_3^{(2)}\Big|_{x_3=h_2};\\
&\varphi^{(1)} = \varphi^{(2)}\Big|_{x_3=h_2}, \quad U_i^{(1)} = U_i^{(2)}\Big|_{x_3=h_2};\\
&\qquad\qquad \cdots\\
&\tau_{3j}^{(m-1)} = \tau_{3j}^{(m)}\Big|_{x_3=0}, \quad D_3^{(m-1)} = D^{(m)}\Big|_{x_3=0};\\
&\varphi^{(m-1)} = \varphi^{(m)}\Big|_{x_3=0}, \quad U_i^{(m-1)} = U_i^{(m)}\Big|_{x_3=0};\\
&\tau_{3j}^{(m)} = 0\big|_{x_3=-h_m}, \quad D_3^{(m)} = D^{(vac)}\Big|_{x_3=-h_m}.
\end{aligned} \tag{3}$$

Here h_m is the thickness of the m-th layer, and X_3 axis coincides with the vertical direction. Substituting the elastic displacements and electric potential taken in the form of linear combinations of n partial waves into the boundary conditions (3) as

$$\begin{aligned}
U_i^{(m)} &= \sum_n C_n^{(m)} \alpha_i^{(n)} \exp\left[i\left(k_1 x_1 + k_3^{(n)} x_3 - \omega t \right)\right],\\
\Phi^{(m)} &= \sum_n C_4^{(m)} \alpha_4^{(n)} \exp\left[i\left(k_1 x_1 + k_3^{(n)} x_3 - \omega t \right)\right],
\end{aligned} \tag{4}$$

one can obtain a matrix of the boundary conditions. Here, $C_n^{(m)}$ and $C_4^{(m)}$ are the amplitude coefficients of elastic displacements and electric potential in the m-th layer, respectively. Equating the matrix determinant to zero forms an algebraic equation determining the characteristics of the elastic wave. The variations of the boundary conditions (3) will define all the types of elastic waves propagating in a layered structure. For example, the first equation in Eq (3) determines propagation of Rayleigh-type waves, and the first and last equations taken at m = 1 describe the propagation of elastic waves in a piezoelectric plate,that is, now Eq (3) can be written as

$$\begin{cases} \sum_{n=1}^{8} C_n \left(C_{3jkl} k_l^{(n)} \alpha_k^{(n)} + e_{k3j} k_k^{(n)} \alpha_4^{(n)} \right) \exp\left(i k_3^{(n)} h \right) = 0, \\ \sum_{n=1}^{8} C_n \left[e_{3kl} k_l^{(n)} \alpha_k^{(n)} - \left(\varepsilon_{3k}^{\eta} k_k^{(n)} - i\varepsilon_0 \right) \alpha_4^{(n)} \right] \exp\left(i k_3^{(n)} h \right) = 0, \\ \sum_{n=1}^{8} C_n \left(C_{3jkl} k_l^{(n)} \alpha_k^{(n)} + e_{k3j} k_k^{(n)} \alpha_4^{(n)} \right) = 0, \\ \sum_{n=1}^{8} C_n \left[e_{3kl} k_l^{(n)} \alpha_k^{(n)} - \left(\varepsilon_{3k}^{\eta} k_k^{(n)} + i\varepsilon_0 \right) \alpha_4^{(n)} \right] = 0. \end{cases} \tag{5}$$

If we assume that the lower layer is thick enough (semi-infinite type), that is, its thickness is much greater than the length of the elastic wave, then in this case the latter equation in Eq. (3) can be ignored, that is, a free bottom border takes place. It is also necessary to require the fulfillment of the condition which provides attenuation of elastic waves in the substrate as $Im\left(k_3^{(m)}\right)<0$. Then the equations describing the propagation of elastic waves in the "layer–substrate" structure will look like

$$\begin{gathered} \sum_{n=1}^{8} \left(a_n C_{3kpi}^{(1)} k_i^{(n)} \alpha_p^{(n)} + a_4 e_{p3k}^{(1)} k_p^{(n)} \alpha_4^{(n)} \right) \exp\left(i k_3^{(n)} h \right) = 0, \\ \sum_{n=1}^{8} \left[a_n e_{3kl}^{(1)} k_l^{(n)} \alpha_k^{(n)} + a_4 \left(\varepsilon_{3p}^{(1)} k_p^{(n)} - i\varepsilon_0 \right) \alpha_4^{(n)} \right] \exp\left(i k_3^{(n)} h \right) = 0, \\ \sum_{m=1}^{4} b_m \left(C_{i3kl}^{(2)} k_l^{(s)} \alpha_k^{(s)} + e_{3pi}^{(2)} k_p^{(s)} \alpha_4^{(s)} \right) - \sum_{n=1}^{8} a_n \left(C_{i3kl}^{(1)} k_l^{(n)} \alpha_k^{(n)} + e_{3pi}^{(1)} k_p^{(n)} \alpha_4^{(n)} \right) = 0, \\ \sum_{m=1}^{4} b_m \left(e_{3kl}^{(2)} k_l^{(s)} \alpha_k^{(s)} + \varepsilon_{3p}^{(2)} k_p^{(s)} \alpha_4^{(s)} \right) - \sum_{n=1}^{8} a_n \left(e_{3kl}^{(1)} k_l^{(n)} \alpha_k^{(n)} + \varepsilon_{3p}^{(1)} k_p^{(n)} \alpha_4^{(n)} \right) = 0, \\ \sum_{s=1}^{4} U_i^{(2)(s)} b_m - \sum_{n=1}^{8} U_i^{(1)(n)} a_n = 0. \end{gathered} \tag{6}$$

Digital superscripts 1 and 2 denote the layer and the substrate, respectively; $\alpha_k^{(s)}$ and b_m are the magnitudes and weight coefficients of s-th partial wave (s = 1, …, 4) in the substrate; $\alpha_k^{(n)}$ and a_n are the magnitudes and weight coefficients of n-th partial wave (n = 1, …, 8) in the piezoelectric layer.

2.2. Dispersive relations for the elastic waves in plates and layered structures

Before investigation of the propagation of elastic waves in a multilayer structure such as "Me1/AlN/Me2/diamond," it makes sense initially to study the marginal cases as propagation of elastic waves in a plate and a layered structure (interlayer interface).

Let us perform the analysis of the characteristics of an acoustic wave in piezoelectric crystalline plate belonging to the point symmetry 23. All the results obtained will be reasonable for other cubic crystals too. In this case, Christoffel tensor Eq. (2) written for the propagation of elastic wave along the [100] direction in (001) plane takes the following form:

$$\Gamma_{il} = \begin{bmatrix} C_{11}k_1^2 + C_{44}^E k_3^2 & 0 & \left(C_{11} + C_{44}^E\right)k_1k_3 & 0 \\ 0 & C_{44}^E\left(k_1^2 + k_3^2\right) & 0 & 2e_{14}k_1k_3 \\ \left(C_{11} + C_{44}^E\right)k_1k_3 & 0 & C_{44}^E k_1^2 + C_{11}k_3^2 & 0 \\ 0 & 2e_{14}k_1k_3 & 0 & -\varepsilon_{11}^{\eta}\left(k_1^2 + k_3^2\right) \end{bmatrix}. \tag{7}$$

Obviously, in this case Γ_{il} tensor can be decomposed into two independent parts, corresponding to the partial wave motion in the X_1X_3 sagittal plane and along the X_2 transverse direction. As usual, the X_1 axis of special Cartesian coordinate system coincides with the wave propagation direction. First part describes a nonpiezoactive Lamb wave, and the second one corresponds to the *SH* acoustic wave possessing the piezoelectric activity.

Characteristic Eq. (7) with respect to k_3 for the Lamb-type wave is a polynomial of the fourth power:

$$\left(C_{11}k_1^2 + C_{44}^E k_3^2 - \rho_0\omega^2\right)\left(C_{44}^E k_1^2 + C_{11}k_3^2 - \rho_0\omega^2\right) - \left(C_{12} + C_{44}^E\right)^2 k_1^2 k_3^2 = 0 \tag{8}$$

Roots of Eq. (8) take the following solutions:

$$k_3^{(n)} = \pm i\sqrt{\frac{1}{2R}\left(P \mp \sqrt{P^2 - 4RQ}\right)}, \tag{9}$$

where $R = C_{11}C_{44}^E$, $P = C_{11}\left(C_{11}k^2 - \varrho_0\omega^2\right) + C_{44}^E\left(C_{44}^E k^2 - \varrho_0\omega^2\right) - \left(C_{11} + C_{44}^E\right)^2 k^2$, $Q = \left(C_{11}k^2 - \varrho_0\omega^2\right)\left(C_{44}^E k^2 - \varrho_0\omega^2\right)$, and $k \equiv k_1$. Eigenvectors corresponding to $k_3^{(n)}$ values can be written as

$$\begin{aligned} k_3^{(1)} &= q_1, & \alpha^{(1)} &= (1,0,p_1,0); \\ k_3^{(2)} &= -q_1 = -k_3^{(1)}, & \alpha^{(2)} &= (1,0,-p_1,0); \\ k_3^{(3)} &= q_3, & \alpha^{(3)} &= (1,0,p_3,0); \\ k_3^{(4)} &= -q_3 = -k_3^{(3)}, & \alpha^{(4)} &= (1,0,-p_3,0); \end{aligned} \tag{10}$$

where $p_1 = -\frac{C_{11}k^2 - \rho_0\omega^2 + C_{44}^E q^2}{(C_{12} + C_{44}^E)k q_1}$ and $p_3 = -\frac{C_{11}k^2 - \rho_0\omega^2 + C_{44}^E q_3^2}{(C_{12} + C_{44}^E)k q_3}$.

Taking Eq. (10) into account, one can obtain the system of Eq. (5) with respect to components $\alpha^{(n)}$ and $k^{(n)}$, and then the determinant can be defined as follows:

$$\begin{bmatrix} Ae^{iq_1h} & -Ae^{-iq_1h} & Be^{iq_3h} & -Be^{-iq_3h} \\ Ce^{iq_1h} & Ce^{-iq_1h} & De^{iq_3h} & De^{-iq_3h} \\ A & -A & B & -B \\ C & C & D & D \end{bmatrix}, \tag{11}$$

where

$$\begin{aligned} p_1 &= -\frac{C_{11}k^2 + C_{44}^E q_1^2 - \rho_0\omega^2}{\left(C_{12} + C_{44}^E\right)kq_1}, \\ p_3 &= -\frac{C_{11}k^2 + C_{44}^E q_3^2 - \rho_0\omega^2}{\left(C_{12} + C_{44}^E\right)kq_3}, \\ A &= C_{44}^E\left(kp_1 + q_1\right); B = C_{44}^E\left(kp_3 + q_3\right), \\ C &= C_{12}k + C_{11}q_1p_1; D = C_{12}k + C_{11}q_3p_3. \end{aligned} \tag{12}$$

Equating to zero the determinant of the matrix (11), one can get the equation describing the propagation for the symmetric mode:

$$\frac{\mathrm{th}\left(\frac{1}{2}iq_3h\right)}{\mathrm{th}\left(\frac{1}{2}iq_1h\right)} = \frac{q_3}{q_1}\frac{\left[C_{11}\left(k^2 - k_l^2\right) - C_{12}q_1^2\right]\left\{C_{12}\left(C_{12} + C_{44}^E\right)k^2 - C_{11}\left[C_{11}\left(k^2 - k_l^2\right) + C_{44}^E q_3^2\right]\right\}}{\left[C_{11}\left(k^2 - k_l^2\right) - C_{12}q_3^2\right]\left\{C_{12}\left(C_{12} + C_{44}^E\right)k^2 - C_{11}\left[C_{11}\left(k^2 - k_l^2\right) + C_{44}^E q_1^2\right]\right\}} \tag{13}$$

and for the antisymmetric mode of Lamb wave [12]:

$$\frac{\mathrm{th}\left(\frac{1}{2}iq_3h\right)}{\mathrm{th}\left(\frac{1}{2}iq_1h\right)} = \frac{q_1}{q_3}\frac{\left[C_{11}\left(k^2 - k_l^2\right) - C_{12}q_3^2\right]\left\{C_{12}\left(C_{12} + C_{44}^E\right)k^2 - C_{11}\left[C_{11}^E\left(k^2 - k_l^2\right) + C_{44}^E q_1^2\right]\right\}}{\left[C_{11}\left(k^2 - k_l^2\right) - C_{12}q_1^2\right]\left\{C_{12}\left(C_{12} + C_{44}^E\right)k^2 - C_{11}\left[C_{11}^E\left(k^2 - k_l^2\right) + C_{44}^E q_3^2\right]\right\}}. \tag{14}$$

Here $k_l = \left(\omega / v_l\right)$ is modulus of the wave vector of the longitudinal bulk acoustic wave, and $q_n \equiv k_3^{(n)}$ is the solution of biquadratic dispersive Eq. (8).

For *SH*-waves, the characteristic dispersive equation similar to Eq. (8) can be written as

$$-\varepsilon_{11}^{\eta}\left[C_{44}^{E}\left(k_1^2+k_3^2\right)-\rho_0\omega^2\right]\left(k_1^2+k_3^2\right)-4e_{14}^2k_1^2k_3^2=0. \tag{15}$$

Solving Eq. (15) with respect to k_3 at the parameter $k \equiv k_1$, one can obtain the result:

$$k_3^{(1,2,3,4)} = \pm i\sqrt{k^2-\frac{1}{2}\left[k_t^2-4k_{14}^2k^2 \pm \sqrt{\left(k_t^2-4k_{14}^2k^2\right)^2+16k_{14}^2k^4}\right]}. \tag{16}$$

Here $k_t = \left(\omega / v_t\right)$ is the modulus of wave vector of the shear bulk acoustic wave, and $k_{14} = \frac{e_{14}}{\sqrt{\varepsilon_{11}^{\eta}C_{44}^{E}}}$ is the electromechanical coupling coefficient (EMCC). Eigenvectors corresponding to a value $k_3^{(n)}$ are equal to

$$\begin{array}{ll} k_3^{(1)} = q_2, & \alpha^{(1)} = \left(0,1,0,p_2\right); \\ k_3^{(2)} = -k_3^{(1)} = -q_2, & \alpha^{(2)} = \left(0,1,0,-p_2\right); \\ k_3^{(3)} = q_4, & \alpha^{(3)} = \left(0,1,0,p_4\right); \\ k_3^{(4)} = -k_3^{(3)} = -q_4, & \alpha^{(4)} = \left(0,1,0,-p_4\right), \end{array} \tag{17}$$

where $p_2 = \alpha_4^{(1)} = \frac{2e_{14}k\,q_2}{\varepsilon_{11}^{\eta}\left(k^2+q_2^2\right)}$, $\quad p_4 = \alpha_4^{(3)} = \frac{2e_{14}k\,q_4}{\varepsilon_{11}^{\eta}\left(k^2+q_4^2\right)}$..

As a result, in this case, the determinant of the boundary conditions (Eq. (5)) is obtained as follows:

$$\begin{bmatrix} Ae^{iq_2h} & -Ae^{-iq_2h} & Be^{iq_4h} & -Be^{-iq_4h} \\ (C+D)e^{iq_2h} & (C-D)e^{-iq_2h} & (E+F)e^{iq_4h} & (E-F)e^{-iq_4h} \\ A & -A & B & -B \\ (C-D) & (C+D) & (E-F) & (E+F) \end{bmatrix}, \tag{18}$$

where

$$A = C_{44}^{E} q_2 + e_{14} k p_2, \quad B = C_{44}^{E} q_4 + e_{14} k p_4, \quad C = e_{14} k - \varepsilon_{11}^{\eta} q_2 p_2,$$
$$D = i\varepsilon_0 p_2, \qquad E = e_{14} k - \varepsilon_{11}^{\eta} q_4 p_4, \qquad F = i\varepsilon_0 p_4. \tag{19}$$

Taking the similar procedure as for the Lamb wave solution, the matrix of the boundary conditions (18) is divided into two independent parts, and the dispersive equations describing the propagation of *SH*-waves could be obtained:

$$\frac{\mathrm{th}(iq_2h)}{\mathrm{th}(iq_4h)} = \frac{q_4}{q_2}\frac{\left[C_{44}^{E}\varepsilon_{11}^{\eta}\left(k^2+q_4^2\right)+2e_{14}^2k^2\right]\left[\varepsilon_{11}^{\eta}\left(k^2-q_2^2\right)+2i\varepsilon_0 q_2\,\mathrm{th}\left(iq_2h\right)\right]}{\left[C_{44}^{E}\varepsilon_{11}^{\eta}\left(k^2+q_2^2\right)+2e_{14}^2k^2\right]\left[\varepsilon_{11}^{\eta}\left(k^2-q_4^2\right)+2i\varepsilon_0 q_4\,\mathrm{th}\left(iq_4h\right)\right]},$$
$$\frac{\mathrm{th}(iq_4h)}{\mathrm{th}(iq_2h)} = \frac{q_4}{q_2}\frac{\left[C_{44}^{E}\varepsilon_{11}^{\eta}\left(k^2+q_4^2\right)+2e_{14}^2k^2\right]\left[\varepsilon_{11}^{\eta}\left(k^2-q_2^2\right)+2i\varepsilon_0 q_2\,\mathrm{cth}\left(iq_2h\right)\right]}{\left[C_{44}^{E}\varepsilon_{11}^{\eta}\left(k^2+q_2^2\right)+2e_{14}^2k^2\right]\left[\varepsilon_{11}^{\eta}\left(k^2-q_4^2\right)+2i\varepsilon_0 q_4\,\mathrm{cth}\left(iq_4h\right)\right]}. \tag{20}$$

It should be noted that in this case the *SH*-wave is also divided into symmetric and antisymmetric modes, which is possible only at the high symmetric directions of elastic wave propagation.

If we need to deposit a thin metal layer on the upper surface of the piezoelectric crystalline substrate without disturbing the mechanical boundary conditions, then the second row of the determinant (18) is changed, which leads to the following new dispersive equation for *SH*-wave:

$$\frac{\mathrm{th}(iq_2h)}{\mathrm{th}(iq_4h)} = \frac{q_4}{q_2}\frac{\left[C_{44}^{E}\varepsilon_{11}^{\eta}\left(k^2+q_4^2\right)+2e_{14}^2k^2\right]\left[\varepsilon_{11}^{\eta}\left(k^2-q_2^2\right)+2i\varepsilon_0 q_2\,\mathrm{th}\left(iq_2h\right)\right]}{\left[C_{44}^{E}\varepsilon_{11}^{\eta}\left(k^2+q_2^2\right)+2e_{14}^2k^2\right]\left[\varepsilon_{11}^{\eta}\left(k^2-q_4^2\right)+2i\varepsilon_0 q_4\,\mathrm{th}\left(iq_4h\right)\right]}$$
$$\times\left(\frac{1+\dfrac{\varepsilon_{11}^{\eta}\left(k^2-q_2^2\right)\mathrm{th}\left(iq_2h\right)+2i\varepsilon_0 q_2}{\varepsilon_{11}^{\eta}\left(k^2-q_2^2\right)\mathrm{cth}\left(iq_2h\right)+2i\varepsilon_0 q_2}}{1+\dfrac{\varepsilon_{11}^{\eta}\left(k^2-q_4^2\right)\mathrm{th}\left(iq_4h\right)+2i\varepsilon_0 q_4}{\varepsilon_{11}^{\eta}\left(k^2-q_4^2\right)\mathrm{cth}\left(iq_4h\right)+2i\varepsilon_0 q_4}}\right) \tag{21}$$

In this case, an additional factor on the right side is the dynamic electromechanical coupling coefficient, depending on the frequency/plate thickness, and taking into account the effect of metallization on the magnitude of the phase velocity of piezoactive *SH*-wave.

Another marginal case is the propagation of an elastic wave when interlayer interface has been taken into account. Let us consider the propagation of the Love wave (*SH*-wave in this case) along the [100] direction in (001) plane of the layered structure as "isotropic dielectric layer/piezoelectric crystalline substrate of 23-point symmetry group." Characteristic equation for *SH*-waves is similar to Eq. (15). Equation (4) for the *SH*-wave in the form of partial waves can be written as

$$U_2 = \left[b^{(1)}\beta^{(1)}\exp\left(q_3^{(1)}x_3\right) + b^{(2)}\beta^{(2)}\exp\left(q_3^{(2)}x_3\right)\right]\exp\left[i\left(kx_1-\omega t\right)\right],$$
$$\Phi = \left[b^{(1)}\exp\left(q_3^{(1)}x_3\right) + b^{(2)}\exp\left(q_3^{(2)}x_3\right)\right]\exp\left[i\left(kx_1-\omega t\right)\right], \tag{22}$$

where

$$\beta^{(1)} = \left.\frac{U_2}{\Phi}\right|_{q_3^{(1)}} = \frac{\varepsilon_{11}^{(S)}\left[k^2 + \left(q_3^{(1)}\right)^2\right]}{2e_{14}^{(S)}kq_3^{(1)}}, \beta^{(2)} = \left.\frac{U_2}{\Phi}\right|_{q_3^{(2)}} = \frac{\varepsilon_{11}^{(S)}\left[k^2 + \left(q_3^{(2)}\right)^2\right]}{2e_{14}^{(S)}kq_3^{(2)}} \tag{23}$$

Here and after the superscript S is marked the substrate material constants. In an isotropic dielectric layer, due to the absence of the piezoelectric effect, the parameters of partial components are $k_3^{(1,2)} = \pm is$ and $k_3^{(3,4)} = \pm ik$, where $s = \sqrt{\frac{\rho_0^{(L)}\omega^2}{C_{44}^{(L)}} - k^2}$. Here and after the superscript L is marked the layer material data. Consequently, the boundary conditions (6) can be written as

$$\begin{gathered}
a^{(3)}\exp\left(ik_3^{(1)}h\right) - a^{(4)}\exp\left(ik_3^{(2)}h\right) = 0, \\
\begin{cases}
a^{(5)}\left(-k_1\varepsilon_{11}^{(L)} + \varepsilon_0\right)\exp\left(ik_3^{(3)}h\right) + a^{(6)}\left(k_1\varepsilon_{11}^{(L)} + \varepsilon_0\right)\exp\left(ik_3^{(4)}h\right) = 0, \\
b^{(1)}\left(C_{44}^{(S)}q_3^{(1)}p_1 + e_{14}^{(S)}k\right) + b^{(2)}\left(C_{44}^{(S)}q_3^{(2)}p_2 + e_{14}^{(S)}k\right) + isC_{44}^{(L)}\left(a^{(4)} - a^{(3)}\right) = 0, \\
b^{(1)}\left(e_{14}^{(S)}kp_1 - \varepsilon_{11}^{(S)}q_3^{(1)}\right) + b^{(2)}\left(e_{14}^{(S)}kp_2 - \varepsilon_{11}^{(S)}q_3^{(2)}\right) + ik\varepsilon_{11}^{(L)}\left(a^{(5)} - a^{(6)}\right) = 0,
\end{cases} \\
b^{(1)}p_1 + b^{(2)}p_2 - a^{(3)} - a^{(4)} = 0, \\
b^{(1)} + b^{(2)} - a^{(5)} - a^{(6)} = 0, \\
p_{1,2} = \frac{\varepsilon_{11}^{(S)}\left[k^2 + \left(q_3^{(1,2)}\right)^2\right]}{2e_{14}^{(S)}kq_3^{(1,2)}}.
\end{gathered} \tag{24}$$

Equating to zero the determinant of Eq. (24), one can get the dispersive equation for the Love wave propagating in the layered structure "isotropic dielectric layer/piezoelectric crystalline substrate" [13]:

$$\begin{gathered}
C_{44}^{(L)}is\,\mathrm{th}(sh) \\
= \frac{AB}{\varepsilon_{11}^{(S)}}\frac{\left[C_{44}^{(S)}\varepsilon_{11}^{(S)}\left(A^2 + k^2\right) + 2\left(\varepsilon_{11}^{(S)}\right)^2k^2\right] - P\left[C_{44}^{(S)}\varepsilon_{11}^{(S)}\left(B^2 + k^2\right) + 2\left(\varepsilon_{14}^{(S)}\right)^2k^2\right]}{B\left(A^2 + k^2\right) - PA\left(B^2 + k^2\right)},
\end{gathered} \tag{25}$$

where $A = q_3^{(1)}$, $B = q_3^{(2)}$, $P = \frac{B}{A}\cdot\frac{\varepsilon_{11}^{(S)}(k^2 - A^2) + 2iA\bar{\varepsilon}}{\varepsilon_{11}^{(S)}(k^2 - B^2) + 2iB\bar{\varepsilon}}$, and $\bar{\varepsilon} = \varepsilon_{11}^{(L)}k\frac{\varepsilon_{11}^{(L)}k\,\mathrm{th}(kh) + \varepsilon_0}{\varepsilon_{11}^{(L)}k + \varepsilon_0\mathrm{th}(kh)}$.

Similar dispersive relation for Love waves (*SH*-waves) for a layered structure "isotropic layer/piezoelectric substrate of hexagonal symmetry" has been obtained in Ref. [14].

2.3. Analysis of anisotropy and dispersion of SAW parameters in "AlN/diamond" PLS

Algorithm for calculating the elastic wave parameters in PLS was based on the method of partial waves, previously well adapted to define the SAW characteristics. To improve the accuracy of calculation, the normalization of Christoffel equations and boundary conditions was applied. Square of EMCC was determined by the relation

$$K^2 = 2\frac{v - v_m}{v}, \tag{26}$$

where v and v_m are SAW phase velocities on the free or metallized surface of the piezoelectric film.

Using data on the elastic properties of diamond [15], and aluminum nitride (AlN) [16], the computer simulations of the SAW propagation in PLS "AlN/(111) diamond" were carried out with options of (100) or (001) on the AlN film orientation. Anisotropy of the Rayleigh wave phase velocity in the (111) plane of the diamond is relatively small, and the (001) plane of AlN film is isotropic with respect to the elastic properties; so, in PLS "(001) AlN/(111) diamond," the SAW propagation is actually happening as on the isotropic medium. In contrast, the "(100) AlN/(111) diamond" PLS gives us an example of noticeable anisotropy in the phase velocity and EMCC.

Determination of what SAW type will be excited in this case is possible, considering the tensor of piezoelectric coefficients for the 6*mm* point symmetry crystal AlN, which has a form in the special Cartesian coordinate system as

$$e'_{l\lambda} = \begin{pmatrix} e_{33} & e_{31} & e_{31} & 0 & 0 & 0 \\ 0 & 0 & 0 & 0 & 0 & e_{15} \\ 0 & 0 & 0 & 0 & e_{15} & 0 \end{pmatrix} \tag{27}$$

Let us choose the SAW propagation X'_2 along the [010] direction in the (100) plane of AlN film. AC electric field vector in accordance with the orientation of IDT will have the $E = (0,\ E_2',\ E_3')$ components located in the sagittal plane. Components of mechanical stress can be found by the relation $\sigma'_{ij} = e'_{nij}E'_n$, where $\sigma'_1 = \sigma'_2 = \sigma'_3 = \sigma'_4 = 0$, $\sigma'_5 = e_{15}E'_3$, and $\sigma'_6 = e_{15}E'_2$. Last component is responsible for pure *SH*-wave (Love wave) excitation. If we consider the SAW propagation along the $X' \,||\, [100]$ axis in the (100) plane of AlN film, it is fulfilled $E = (E'_1,\ 0,\ E'_3)$, , and stress components are of the form: $\sigma'_1 = e_{33}\acute{E}_1$, $\sigma'_2 = e_{31}\acute{E}_1$, $\sigma'_3 = e_{31}\acute{E}_1$, $\sigma'_5 = e_{15}\acute{E}_3$, and $\sigma'_4 = \sigma'_6 = 0$. Components σ'_1 and σ'_5 are responsible for the excitation of longitudinal and transverse components of the

partial waves of the Rayleigh SAW; σ'_2 and σ'_3 are associated with parasitic BAW excitation. Consequently, for a given orientation, the possibility of piezoelectric *SH*-wave excitation is absent. In principle, this situation is analogous to the case of the (001) orientation of the AlN film, in which at any IDT location the Rayleigh SAW will only be excited.

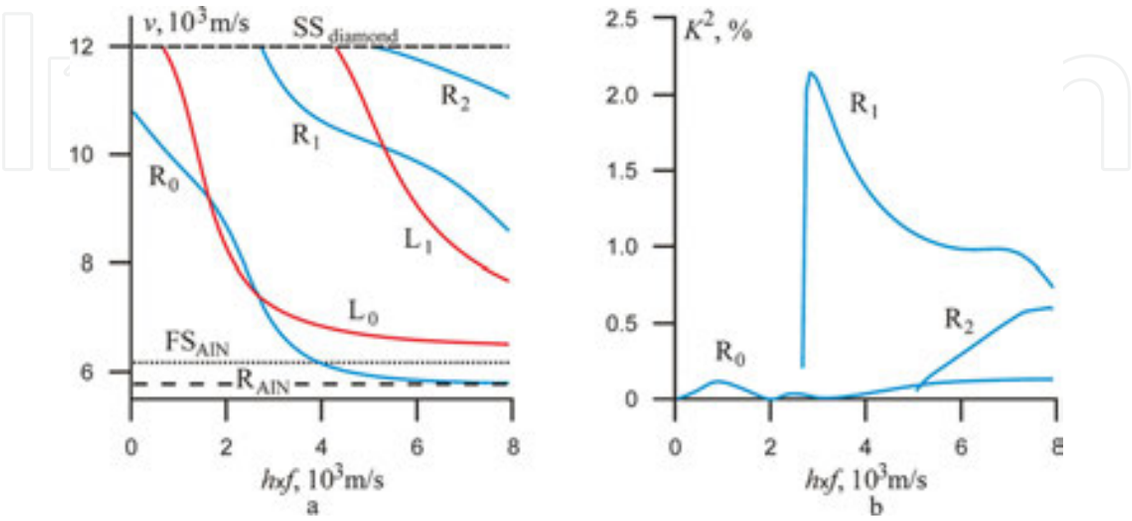

Figure 1. Dispersion dependences of SAW phase velocities (a) and EMCCs (b) versus the $h \times f$ product for the "(001) AlN/(111) diamond" piezoelectric layered structure. Fast and slow bulk acoustic waves are designated as *FS* и *SS*, respectively. Curves $R_0 - R_2$ and L_0, L_1 are associated with the Rayleigh and Love surface acoustic waves.

Dispersion curves of SAW phase velocities and EMCCs for the "(001) AlN/(111) diamond" PLS depending on the $h \times f$ product are shown in **Figure 1**. Here, h is the AlN film thickness. Phase velocity of the fundamental R_0 Rayleigh wave is changed from 10844 m/s (Rayleigh wave propagating in the (111) diamond plane at $h = 0$) up to 5775 m/s (Rayleigh wave propagating in the (001) plane of AlN film at $h \to \infty$). Phase velocity of the lowest L_0 Love mode is changed from 11992 m/s (*SS* mode in diamond) up to 6511 m/s at $h \times f = 8000$ m/s tending to *FS* phase velocity in AlN film, which is equal to 6398 m/s. As one can see, the only Rayleigh waves can be excited by piezoelectric effect because their EMCCs have non-zero values, but the excitement of *SH*-waves should be absent (**Figure 2b**). Maximal value of $K^2 = 2.1$ % with $h \times f = 2900$ m/s will be observed for the R_1 mode which is often called as Sezawa wave. These dependences are qualitatively close to those obtained by the authors [17].

Dispersion curves of SAW phase velocities and EMCCs versus the $h \times f$ product for the "(100) AlN/(111) diamond" PLS are shown in **Figure 2**. In this case, there is a significant anisotropy of the elastic and piezoelectric properties of AlN film; therefore, it is necessary to specify a definite direction of wave propagation. Phase velocity of the R_0 mode is changed from 10787 up to 5884 m/s (Rayleigh wave propagating in the (100) plane of AlN film along the [010] direction at $h \to \infty$). Phase velocity of the lowest L_0 mode is changed from 11992 up to 6282 m/s, tending to *SS* phase velocity in AlN film, which is equal to 6172 m/s. In this direction only *SH*-waves can be excited by a piezoelectric effect. On the other hand, the excitation of Rayleigh

http://dx.doi.org/10.5772/62630

waves should be absent (**Figure 2b**). Maximum value of $K^2 = 0.76$ % will be observed for the L_0 mode at $h \times f = 2050$ m/s. Obtained dependences are qualitatively close to the similar ones [18].

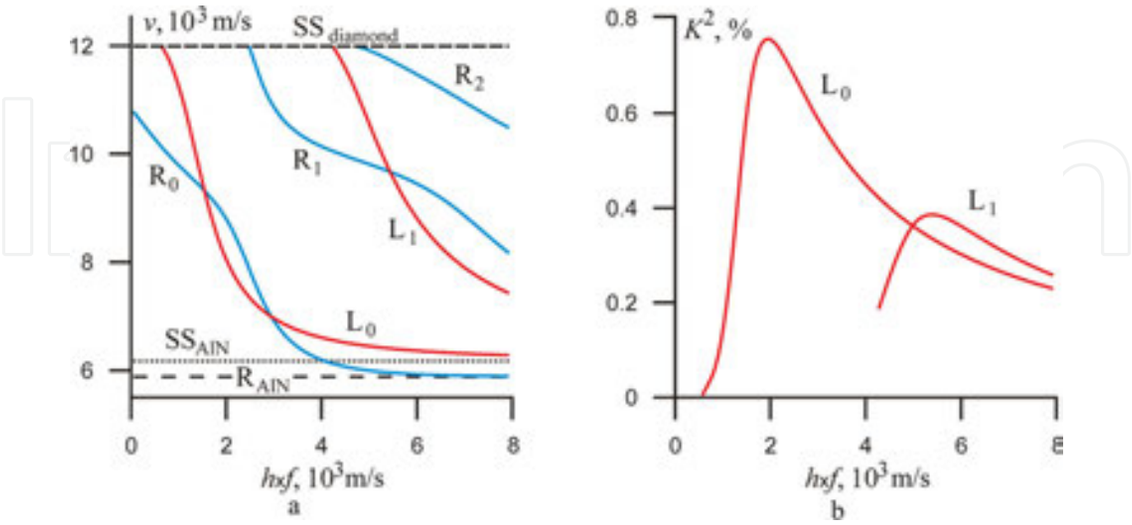

Figure 2. Dispersion dependences of SAW phase velocities (a) and EMCCs (b) versus the $h \times f$ product for the "(100) AlN/(111) diamond" PLS. SAW propagation was chosen along the [010] direction of AlN film and coincided with the direction $[11\bar{2}]$ in (111) diamond plane.

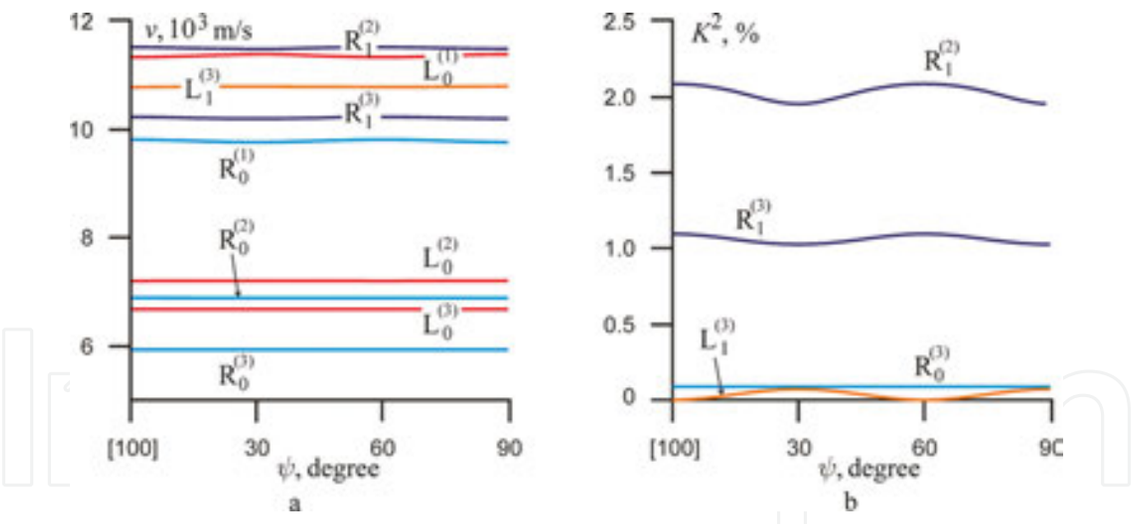

Figure 3. Anisotropy of SAW phase velocity (a) and EMCC (b) in the "(001) AlN/(111) diamond" PLS at different values of $h \times f$ (m/s): (1) 1000; (2) 3000; (3) 5000.

Figure 3 represents the anisotropy of SAW parameters in the "(001) AlN/(111) diamond" PLS. A set of curves is associated with data for the three values of the $h \times f$ product. Investigated structure shows the highest EMCC for the Rayleigh-type waves and low anisotropy of the phase velocity due to weak anisotropy of elasticity in the (111) diamond plane. Thus, high-velocity Sezawa mode R_1 has the maximal value $K^2 = 2.1$ %, and the phase velocity of 11531 m/s at $h \times f = 3000$ m/s.

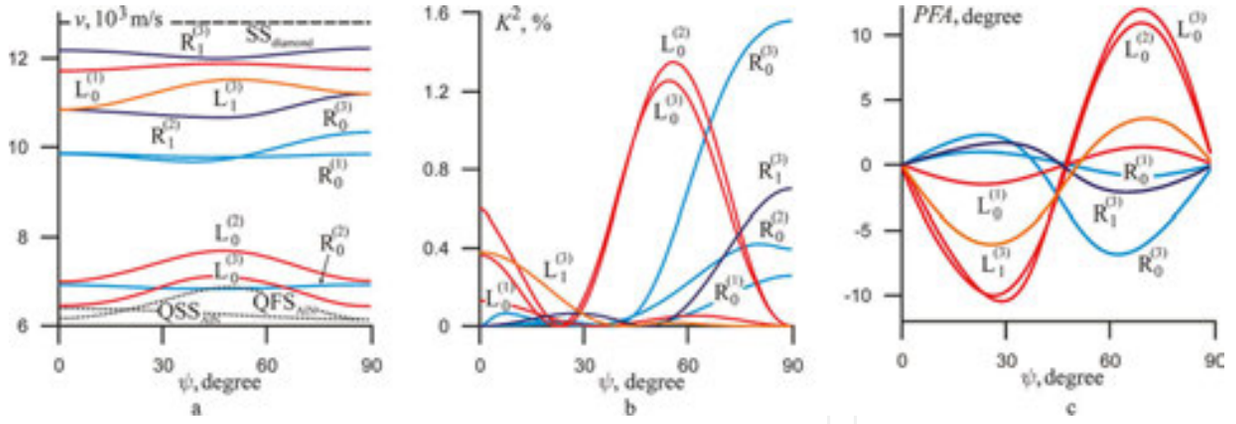

Figure 4. Anisotropy of SAW phase velocity (a), EMCC (b), and PFA (c) in the "(100) AlN/(111) diamond" PLS at different values of $h \times f$ (m/s): (1) 1000; (2) 3000; (3) 5000. Angle ψ was measured from the [010] up to [001] direction in the (100) plane of the AlN film. The [010] direction of AlN film coincided with the $[11\bar{2}]$ direction in (111) diamond plane.

Figure 4 shows the anisotropy of SAW parameters in the "(100) AlN/(111) diamond" PLS. As follows from **Figure 4b**, best EMCC values of 1.6 and 0.7% have a fundamental Rayleigh mode R_0, and Sezawa mode R_1 at $h \times f$ = 5000 m/s in the [001] propagation direction of AlN film (ψ = 90 °). Sezawa mode has also the greatest value of the phase velocity of 12290 m/s (**Figure 4a**). Note that in this direction a propagation of the pure modes will be realized both for the Rayleigh and *SH*-type waves (**Figure 4c**), because power flow angle (PFA) tends to zero, but only Rayleigh modes can be excited due to the AlN piezoelectric effect. Love wave has a maximal EMCC K^2 = 1.35 % in the direction ψ = 56 °, but it is no longer a pure mode.

3. Experimental Investigations of Acoustic Wave Excitation and Propagation in Diamond Based PLSs

3.1. Objects of Investigation

The IIa-type synthetic diamond single crystals grown by HPHT method at the Technological Institute for Superhard and Novel Carbon Materials were used as substrates for the studied PLSs. All the substrate specimens were double-side polished up to the roughness *Ra* lower than 15 nm on 10 × 10 μm² surface controlled by AFM method. Metal electrodes and AlN piezoelectric films were deposited by magnetron sputtering equipment AJA ORION 8. A preferred choice of Mo as a bottom electrode is explained by a good accordance between acoustical impedances of diamond and Mo. It can be seen by the X-ray diffraction pattern for the test sample AlN/Mo/glass (**Figure 5**) that the AlN film has the preferred orientation (002), and the full-width at half-maximum for this reflection is 0.213°. The X-ray diffraction measurements were performed by Empyrean (Panalytic) equipment. **Figure 5** shows SEM images of the surface and cross-section of the AlN/Mo/Si test sample. One can see the surface morphology of the AlN film with a crystallite size about 30–100 nm. The SEM investigations were performed by the JSM-7600F (JEOL) high-resolution scanning electron microscope. The PLS

http://dx.doi.org/10.5772/62630

fabrication technology was in detail described in Ref. [19]. Electrode structures with a specified topology were deposited using both masks and photolithography by the Heidelberg μPG 101 equipment. Explosive photolithography was necessary to form a specified AlN film topology. The thickness of deposed films varied within 150–200 nm for top electrode, 0.4–5.5 μm for AlN piezoelectric layer, and 150–200 nm for bottom electrode. The set of the studied PLSs is represented in **Table 1**.

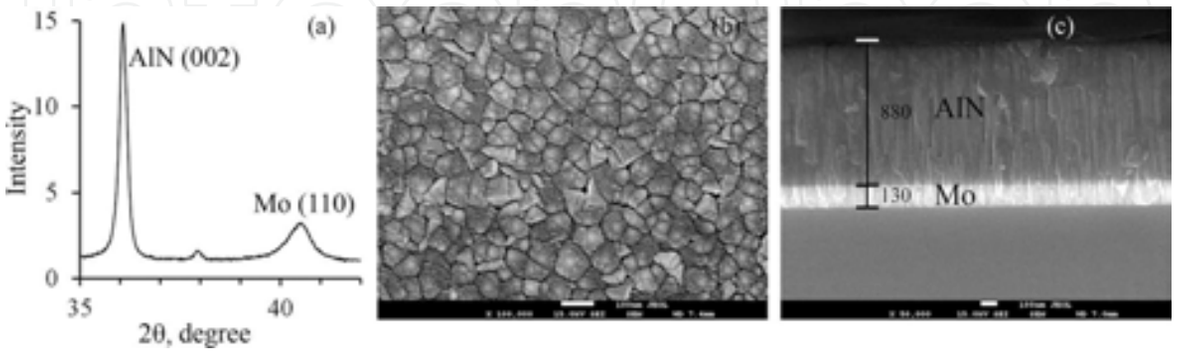

Figure 5. (a) X-ray diffraction pattern of AlN/Mo/glass test sample; (b) SEM images of AlN surface (magnification ×100,000); (c) SEM cross-section image (magnification ×50,000) of AlN/Mo/Si test sample.

PLS #	PLS composition	Material/thickness (nm) of top electrode	Thickness (μm) of AlN film	Material/thickness (nm) of bottom electrode	Thickness (μm) of (100) diamond substrate
1	Al/AlN/Mo/(100) diamond	Al/250	3.1	Mo/200	1037
2	The same	Al/250	1.04	Mo/150	137
3	The same	Al/164	0.624	Mo/169	392
4	Al/AlN/Mo/Pt/(100) diamond	Al/200	1.044	Mo/115 Pt/10	501
5	Pt/AlN/Pt/(100) diamond	Pt/250	1.04	Pt/177	460
6	Al/AlN/Mo/(100) diamond	Al/200	3.2	Mo/200	1040
7	The same	Al/200	1.04	Mo/150	303
8	Pt IDT/AlN/(100) diamond	Pt/156	5.53	–	1040

Table 1. Set of studied PLSs.

The influence of area size and the shape of the electrodes on the signal quality was studied. Serial number of resonator's notation is associated with the shape, while the letter represents the area of the top electrode. Here #"1" means a pentagon form, #"2"–irregular rectangle, and #"3"–circular form. The area of electrode "a" is 40000, "b"–22500, and "c"–10000 μm^2. All these 1a–3c electrodes are associated with different HBARs with the same AlN and metal layers.

3.2. UHF study of acoustic wave excitation and propagation in piezoelectric layered structures

Microwave studies of PLSs were carried out by equipment (**Figure 6**) comprising the E5071C network analyzer (300 kHz–20 GHz) and the M-150 probe station. The experiments were fulfilled in the reflection mode with a test device connected by ACP40-A-SG-500 probe (the distance between tips was equal to 500 μm). **Figure 7** shows the photograph of one of the studied samples (PLS #3).

Figure 6. Experimental setup: E5071C network analyzer, M-150 probe station, and studied diamond-based PLS.

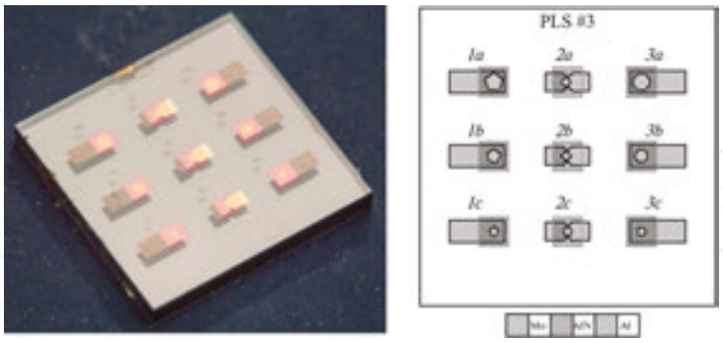

Figure 7. General view of the PLS#3 included nine acoustic resonators.

3.3. PLS microwave acoustic properties measuring: phase velocities, quality factor and quality parameter, frequency and temperature dependences

PLS gives us a unique possibility to investigate the acoustic properties within a wide frequency band from several MHz up to tens of GHz: from fundamental $\lambda/2$ resonance ($n = 1$) up to UHF

overtones ($n > 1000$). Really, in the successful observation, all the overtones will depend on the quality and thickness of TFPT, and even more the acoustic attenuation in the substrate as well as the quality of their preparation. **Figure 8** represents frequency dependence of S_{11} parameter (reflection coefficient) measured close to first acoustic overtone (f_{1r} = 8.39543 MHz) of the PLS #1. The quality factor Q of an oscillator can be measured as

$$Q = \frac{f_{nr}}{\Delta f} \tag{28}$$

where f_{nr} is the resonant frequency of n-th overtone of BAW longitudinal type (L), and Δf is the bandwidth measured at −3 dB level. The second method for determining the Q factor was based on the relation

$$Q_{n,\tau_d} = \frac{1}{2}\omega_{p,n}\left|\frac{d\varphi_n}{d\omega_{p,n}}\right| = \pi\tau_d f_{p,n} \tag{29}$$

where $\omega_{p,n} = 2\pi f_{p,n}$, φ_n is the phase shift angle, and τ_d is the group delay time. However, since the experimentally obtained values of Q from Eqs. (28) and (29) have only a slight difference, we will further use only Eq. (28) for Q calculations.

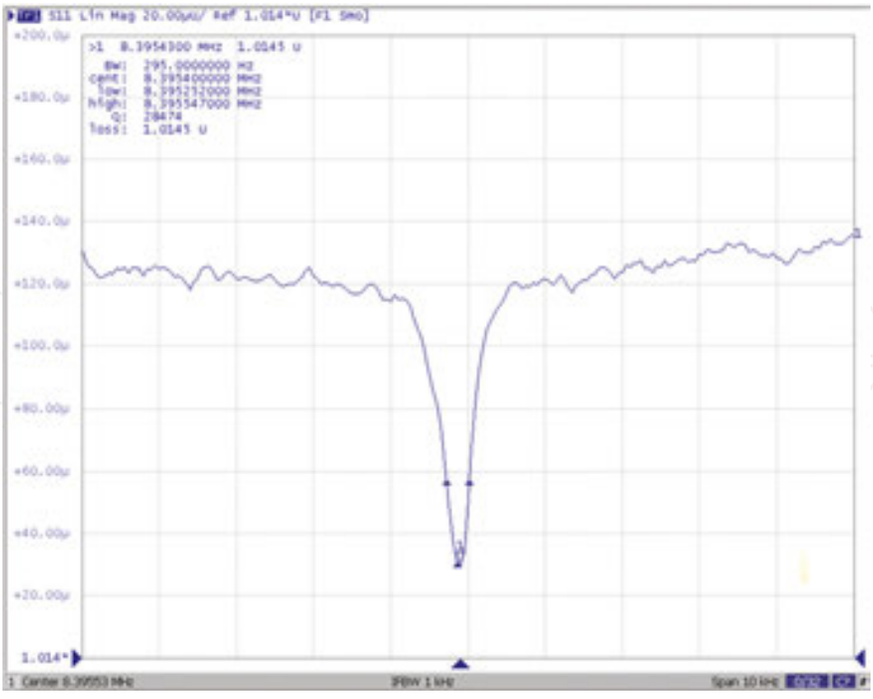

Figure 8. Frequency dependence of S_{11} parameter close to first acoustic overtone (f_{1r} = 8.39543 MHz, and Q = 28754) of the PLS #1.

The resonant frequencies of PLS can be calculated approximately by the relation:

$$f_{nr} \approx n\frac{v_l}{2h}, \tag{30}$$

where v_l is the longitudinal BAW phase velocity, and h is the substrate thickness. Calculation of phase velocity for [100] diamond at a given thickness gives us v_l = 17412 m/s which is close to known data 17542 m/s, obtained by acoustic echo pulse method [7]. Error of ~0.7 % can be explained by TFPT loading and phase shifts in layers.

Note that the resonance phenomena at low frequencies in PLS will be realized with low TFPT effectiveness.

It was found that such parameter as impedance Z_{11} is more convenient than S_{11} reflection coefficient for the analyzing of PLS acoustic properties. In order to get a proper measurement of a Q factor, one needs to obtain a value for a "pure," or extracted, impedance of PLS [20]. First, we measure an absolute value of total impedance Z_{11} at the resonant frequency. Then, the value of the extracted impedance $|Z_{11e}|$ can be calculated as

$$|Z_{11e}| = |Z_{11}| - |Z_{11}^{'}|, \tag{31}$$

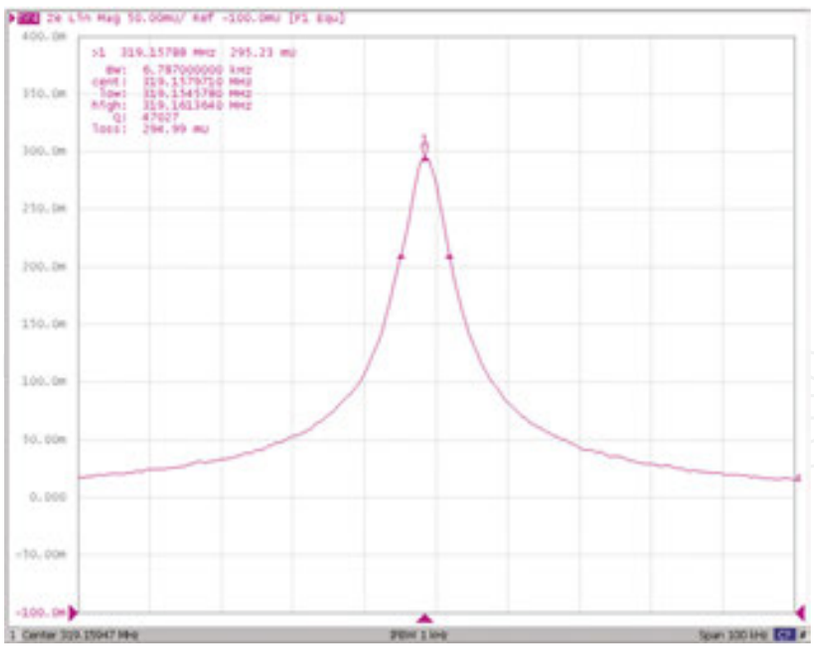

Figure 9. Frequency dependence of the extracted impedance $|Z_{11e}|$ close to fifth acoustic overtone (f_{5r} = 319.157971 MHz, and Q = 47027) of the PLS #2.

where $|Z_{11}^{'}|$ should be measured in the frequency area away from the acoustic resonance. Only after this procedure, the proper Q value should be calculated accurately taking $|Z_{11e}|$ magni-

http://dx.doi.org/10.5772/62630

tudes on the -3 dB level. As an example, frequency dependence of the extracted impedance $|Z_{11e}|$ close to fifth acoustic overtone of PLS #2 is presented in **Figure 9**.

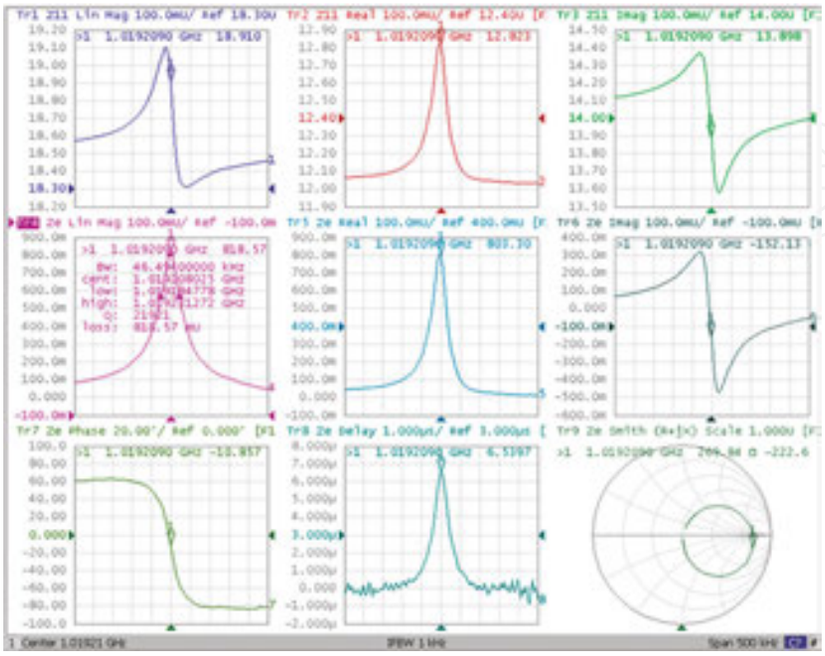

Figure 10. Frequency dependence of a number of measured PLS parameters close to 16th acoustic overtone (f_{16r} = 1.019209 GHz, and Q = 21921) of the PLS #2.

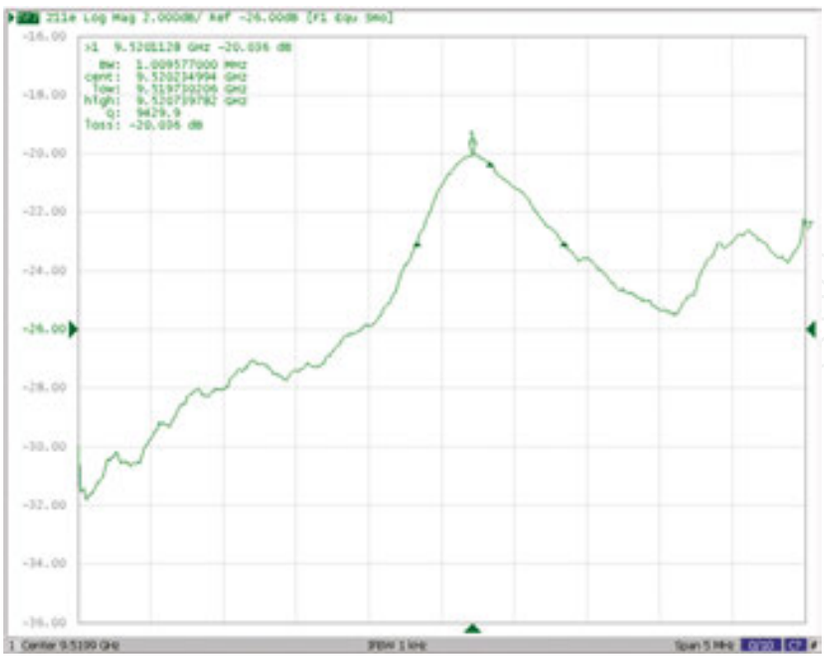

Figure 11. Frequency dependence of the extracted impedance $|Z_{11e}|$ close to 425th acoustic overtone (f_{425r} = 9.520235 GHz and Q = 9430) of the 1b resonator PLS #3.

A full view of a number of measured PLS parameters such as Z_{11}, Z_{11} Real, Z_{11} Imag, Z_e, Z_e Real, Z_e Imag, Z_e Phase, Z_e Delay, and Smith diagram is presented in **Figure 10** close to 16th acoustic overtone of the PLS #2. As one can see, the PLS #2 has a high Q = 21921 at ~1 GHz of operational frequency. Note that Z_e phase parameter is convenient in determining the resonant frequency when phase shift is equal to zero. Smith diagram gives us a full screen of the impedance within the given frequency band. For example, this option is convenient when the matching of a device and a measuring circuit should be executed.

Frequency dependence of the extracted impedance $|Z_{11e}|$ close to 425th acoustic overtone of the 1b resonator (PLS #3) is represented in **Figure 11**. Note that a high Q = 9430 was obtained at an operational frequency ~10 GHz.

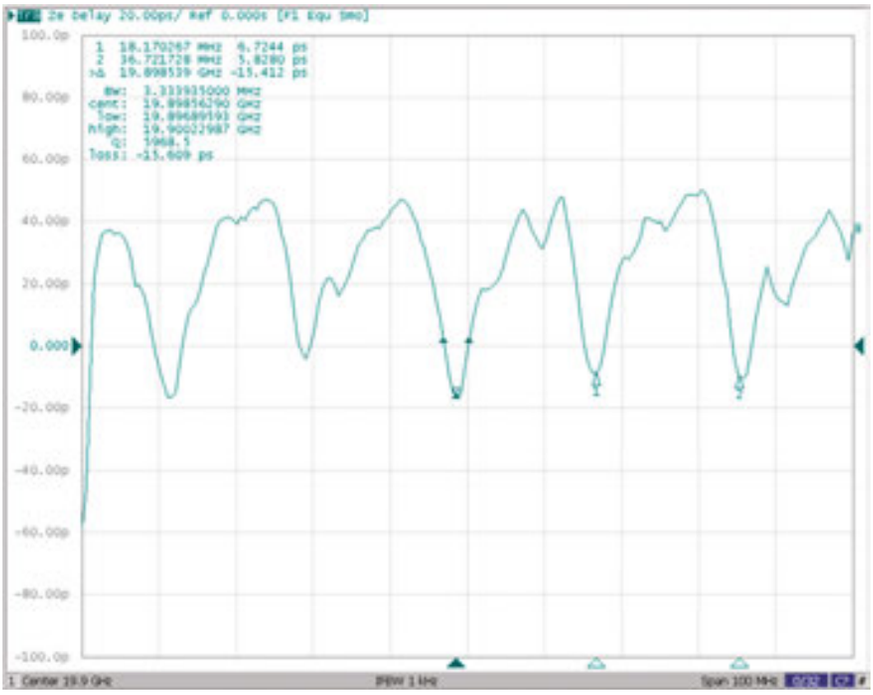

Figure 12. Frequency dependence of the extracted impedance Z_e delay close to 1137th acoustic overtone (f_{1137r} = 19. 8985629 GHz and Q = 5969) of the PLS #4.

Resonant peak at extreme operational frequency combining with high Q value was obtained at 1137th acoustic overtone (f_{1137r} = 19. 8985629 GHz and Q = 5969) of the PLS #4 (**Figure 12**). Note that operational frequency belongs to *K*-band, and as a result the diamond-based PLS can be realized as acoustoelectronic devices efficient at such frequencies.

Analyzing the data on the frequency dependence of Q factor within a wide frequency band (**Figure 13**), a nonmonotonic Q is noted, decreasing with respect to a frequency increment. The reason for the appearance of local maximums and minimums will be discussed below (Section 4.2). But it is more convenient to represent experimental data by quality parameter as $Q \times f$ product. The main purpose of such representation is that the phonon–phonon attenuation in the crystals is often represented as $Q \times f = f(\omega)$ relation in order to define the mechanism of

http://dx.doi.org/10.5772/62630

UHF acoustic attenuation. Detailed investigation of the frequency dependence of quality parameter for the nine resonators (PLS #3) was carried out, and the experimental results in part are represented in **Figure 14**. Here, rather high values of Q (up to 35000) at low frequencies take place, while increasing frequency results in decreasing Q factor with ~10000 at 9–10 GHz. Individual resonators differed from one another by configuration and square. As one can see, the best top electrode configuration in terms of higher $Q \times f$ (and Q) seems to be the irregular rectangular form. This result is more sufficient at high frequencies and low top electrode area size.

Analyzing **Figure 14**, an unusual frequency dependence of $Q \times f$ quality parameter was found as far as $Q \times f$ has increased at higher frequencies running up to $Q \times f \sim 10^{14}$ Hz. Such value for diamond is one of the highest among known materials, but for the first time it was obtained at ~10 GHz operational frequency.

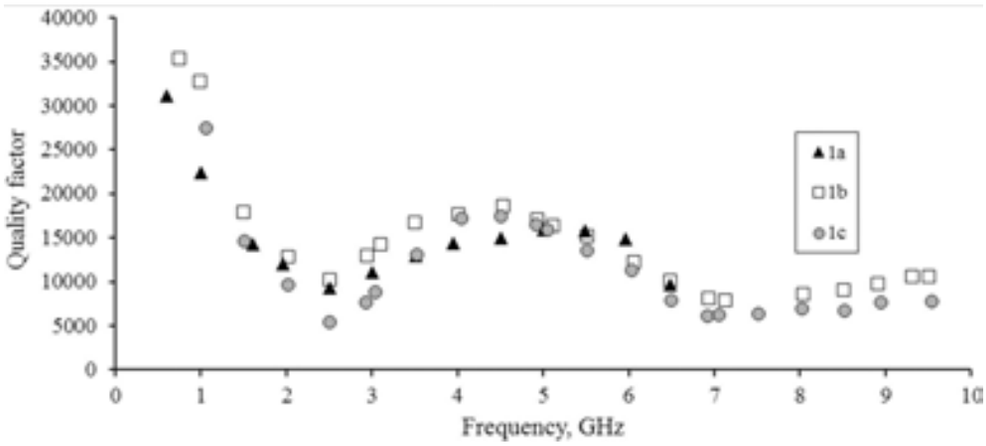

Figure 13. Frequency dependence of Q factor for 1a, 1b, and 1c resonators (PLS #3, see **Figure 7** and Section 3.1).

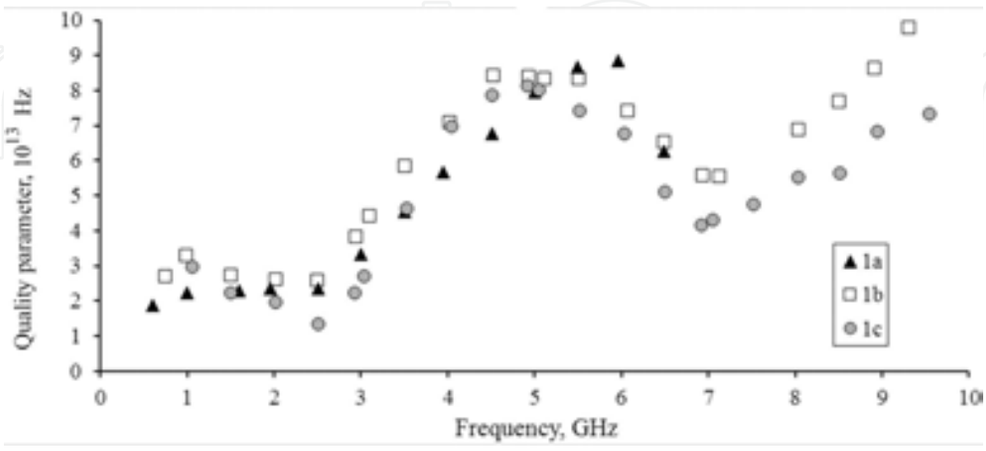

Figure 14. Frequency dependence of quality parameter $Q \times f$ for a set 1a, 1b, and 1c resonators with different top electrode area and shape (PLS #3, see **Figure 7** and Section 3.1).

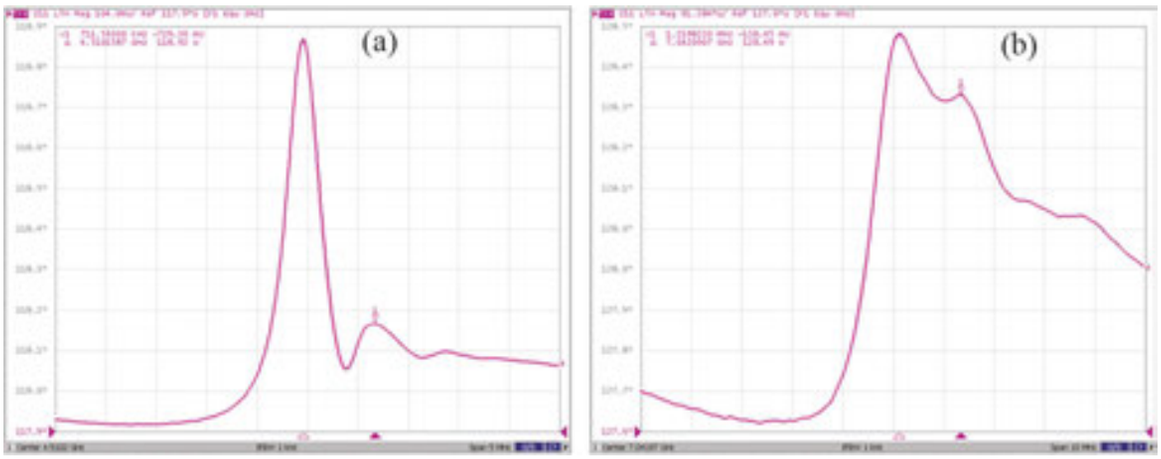

Figure 15. Frequency dependence of Z_{11} impedance for 1a resonator of PLS #3 measured close to 4.5 (a) and 7 (b) GHz.

Because the PLS in comparison with conventional piezoelectric resonator is an inhomogeneous acoustical device, a lot of unwished waves can be excited, distorting sometimes a useful signal. As an example here, we will focus only on 1a resonator (PLS #3). The amplitude–frequency characteristic (AFC) for this resonator is represented in **Figure 15**. As one can see, at rather low frequencies the main resonant peak has a number of adjacent so-called spurious peaks, which are placed at slightly higher frequencies. Such spurious peaks have lower amplitudes and are located at a certain distance away from the resonant signal. In this case, they have no influence on the main peak and its Q value (**Figure 15a**). However, increasing the resonant frequency can result in a convergence of such peak to a resonant signal, and some distortion of a useful signal takes place (**Figure 15b**).

Study of temperature dependence on resonant frequency for diamond-based PLS is also of great practical importance. The experimental results on the temperature dependence of normalized frequency

$$\frac{\Delta f}{f_r} = \frac{f_r(T) - f_r(20\ \ )}{f_r(20\ \ )}, \tag{32}$$

where $f_r(20°C)$ is the resonant frequency at $T = 20°C$ (at room temperature) are represented in **Figure 16** for the PLS #5 for two resonant frequencies close to 1 GHz in a wide temperature range. As one can see, the normalized frequency has monotonic temperature dependence with low slope at low-temperature region. Temperature coefficient of frequency (TCF) can be defined as

$$TCF = \frac{1}{40^{\circ}} \frac{f_r(40\ \ ) - f_r(0\ \ )}{f_r(20\ \ )}. \tag{33}$$

http://dx.doi.org/10.5772/62630

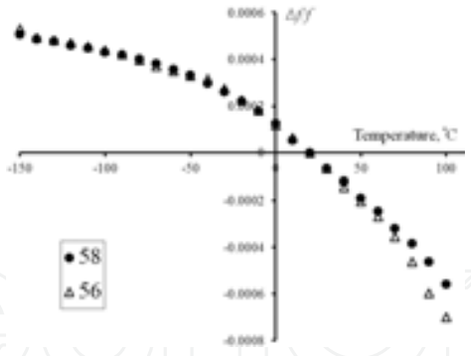

Figure 16. Temperature dependence of $\Delta f/f_r$ for the PLS #5 were measured on resonant frequencies f_{58r} = 1101 and f_{56r} = 1063 MHz associated with 58th and 56th overtones, respectively.

For a number of studied PLSs, the TCFs at different frequencies are represented in **Table 2**. The obtained TCF values were in a range$(-4.5\text{to} - 6.5) \times 10^{-6} K^{-1}$.

PLS#	Resonant frequency, MHz	TCF, 10^{-6} K^{-1}
5	1101.328	−6.14
	1063.420	−6.54
6	596.028	−4.53
	612.718	−4.63
7	722.325	−4.50
	751.273	−4.84

Table 2. TCF for a number of studied PLSs at different frequencies.

The typical temperature dependence of *Q* factor for the PLS #6 is represented in **Figure 17** for a temperature range −100 to 100C. Note that the quality factor decreases while temperature increases.

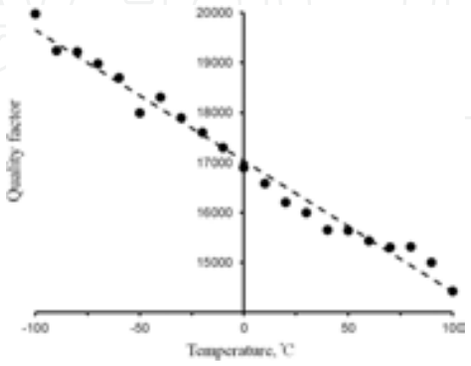

Figure 17. Quality factor's temperature dependence for the PLS #6 measured at resonant frequency ~596 MHz (71st overtone).

In order to excite the SAW, a special interdigital transducer (IDT) should be formed. Study of SAW propagation was carried out by means of a delay line as the "Pt IDT/AlN/(001) diamond" PLS #8 (**Figure 18**). Here, one can see two identical SAW delay lines based on (100) diamond substrate 4 × 4 mm^2, and including IDTs (period d_{IDT} = 10 μm, and aperture 500 μm) on the top of the AlN surface. The thickness of the AlN film (~5.5 μm) was chosen to satisfy the condition of effective SAW excitation on the 500–700 MHz range. Therefore, the SAW of Rayleigh-type was propagated along the [110] direction of diamond and simultaneously within the AlN film. In such PLS, the conditions for a number of Rayleigh-type surface waves of different orders could be realized, for example, R_0, R_1, and so on.

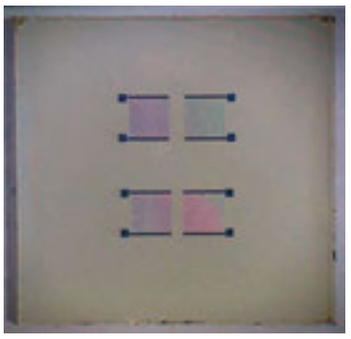

Figure 18. General view of the PLS #8 (d_{IDT} = 10 μm).

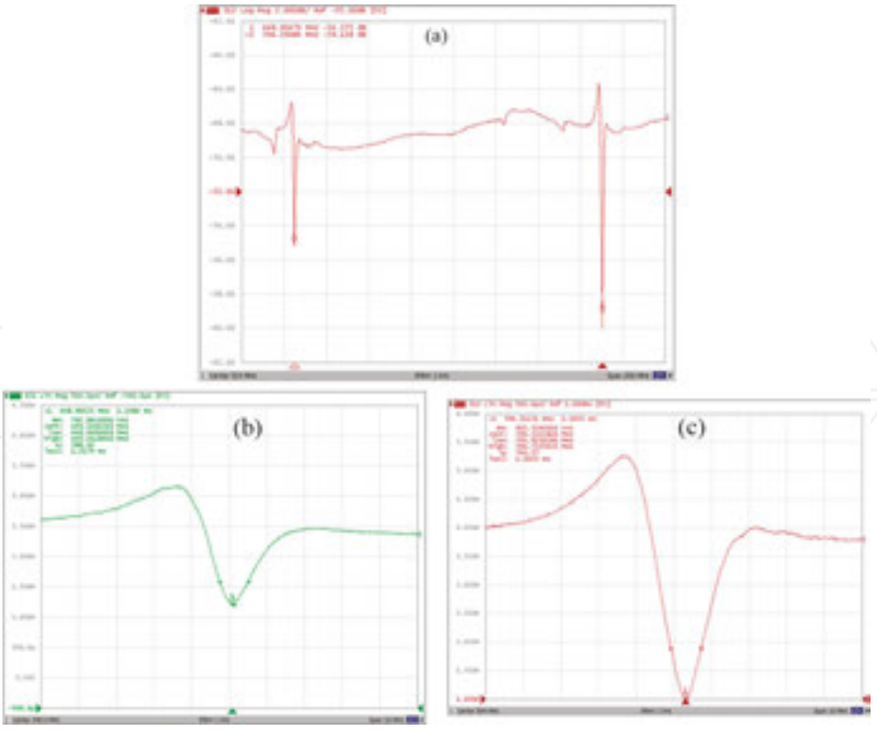

Figure 19. Amplitude–frequency characteristic of SAW propagating in the PLS #8 along [110] direction of diamond: (a) AFC general view; (b) R_0 mode; (c) R_1 mode.

The AFC of the PLS #8 is shown in **Figure 19**. There are two resonant peaks: at 449 MHz (fundamental Rayleigh mode R_0) and at 594 MHz (Sezawa mode R_1). Such modes are shown on **Figure 19b** and **c**.

3.4. UHF acoustic attenuation in diamond

The results on the frequency dependence of quality parameter can be explained in terms of acoustic attenuation. There are many different mechanisms of acoustical energy losses in PLS. Careful study shows that the attenuation in a rather thick diamond substrate is much higher than the one for thin electrode and AlN film [10]. The influence of roughness losses of AlN film and diamond can be estimated as [20]:

$$\alpha_R \approx 2\pi \cdot 8.68\left(k_{\mathrm{AlN}}^2 \eta_{\mathrm{AlN}}^2 + k_{\mathrm{diam}}^2 \eta_{\mathrm{diam}}^2\right)N, \tag{34}$$

where k_{AlN}, k_{diam}, η_{AlN}, and η_{diam} are the wave vectors and root-mean-squared roughnesses for AlN and diamond, respectively, and N is the number of reflections of an acoustic wave in a sample per 1 s. For studied samples with $\eta_{\mathrm{AlN}} < 30$ nm and $\eta_{\mathrm{diam}} < 15$ nm it can be shown that acoustic attenuation contributions concerned with roughness are estimated as: $\alpha_{R(\mathrm{AlN})} \approx 0.164\mathrm{dB/(GHz^2{\times}cm)}$ and $\alpha_{R(\mathrm{diam})} \approx 0.0035\mathrm{dB/(GHz^2{\times}cm)}$. An extremely low value of damaged layer arising as a result of mechanical polishing of diamond surface was estimated by Kikuchi lines observation [21] as ~30 nm, which is an extremely low value, and has almost no influence on the full acoustic attenuation.

Fundamental origin of acoustical attenuation in solids is defined by phonon–phonon interaction, which can be concerned with two different mechanisms. At relatively low frequencies, when $\omega\tau_{th} \ll 1$ (τ_{th} is the time of thermal relaxation for phonon–phonon interaction) Akhiezer's mechanism should take place [22], while at relatively high frequencies ($\omega\tau_{th} \gg 1$) it should be replaced by Landau–Rumer's mechanism [23]. For such attenuation mechanisms, the quality parameter and acoustic attenuation have a form adapted for PLSs operating by longitudinal BAW [10,24]:

$$\left.\begin{aligned} \alpha_{ph-ph} &= \frac{8.68\pi C_V T\gamma^2\tau_{th}}{\varrho_0 v_l^3\left[1+\left(2\pi f\tau_{th}\right)^2\right]} f^2 \\ Q\times f &= \frac{\varrho_0 v_l^2\left[1+\left(2\pi f\tau_{th}\right)^2\right]}{C_V T\gamma^2\tau_{th}} \approx \mathrm{const} \end{aligned}\right\} \text{Akhiezer regime,}$$

$$\left.\begin{aligned} \alpha_{ph-ph} &= \frac{8.68\pi^5\gamma^2\left(k_B T\right)^4}{30\varrho_0 v_l^6 h^3} f \\ Q\times f &= \frac{30\varrho_0 v_l^5 h^3}{\pi^4\gamma^2\left(k_B T\right)^4} f \end{aligned}\right\} \text{Landau--Rumer regime.} \tag{35}$$

Here, C_V is the specific heat per volume unit, γ is Grüneisen parameter, k_B and h are the Boltzmann and Planck's constants, respectively. As one can see, the main difference between

Akhiezer and Landau–Rumer mechanisms is the frequency dependence of attenuation and quality parameter. For example, the $Q \times f$ should have no frequency dependence at the Akhiezer regime, while at Landau–Rumer regime, the $Q \times f$ should be increased proportionally to the frequency. Estimation of acoustic attenuation by Eq. (35) within the frequency range 0.3–10 GHz gives a much higher value than that due to the contributions of roughness taking place on the AlN and diamond surfaces. Thereby, the most significant influence on the resulted acoustic attenuation arises from phonon–phonon interactions. Experimental results of the frequency dependence of quality parameter for a number of diamond-based PLSs are represented in **Figure 20**.

As seen from **Figure 20**, the quality parameter has almost no frequency dependence while $f <$ 1 GHz, and after that it has a linear growth, which can be explained as the change of the attenuation mechanism at ~1 GHz from Akhiezer's to Landau–Rumer's. Comparing the experimental results from **Figure 20** with the analytical expressions from Eq. (35), the thermal relaxation time and Grüneisen parameter for longitudinal bulk acoustic wave propagating along the [100] direction of diamond can be estimated as 3.5×10^{-10} s and 0.85, respectively. Note that here we used particular Grüneisen parameter for the longitudinal mode since it can be different for different acoustic modes in crystal. Finally, for IIa diamond single crystal at Akhiezer regime ($f < 1$ GHz), $Q \times f \approx 1.8 \times 10^{13}$ Hz and $\alpha_{ph-ph} \approx 0.9 \times f^2$ dB/(GHz^2×cm), while for Landau–Rumer regime, $Q \times f \approx 1.8 \times 10^4 \times f$ Hz and $\alpha_{ph-ph} \approx 0.9 \times f$ dB/(GHz×cm). Frequency about 1 GHz is an extremely low value for the change of phonon–phonon interaction mechanism: all the known crystals applied in acoustoelectronics have such a change at much higher frequencies (20 GHz and higher). This result means that diamond crystal may be a promising substrate for acoustoelectronic devices when the operating frequency should be higher than the units of GHz. UHF acoustic attenuation in diamond in comparison with other commonly used crystals is represented in **Table 3**.

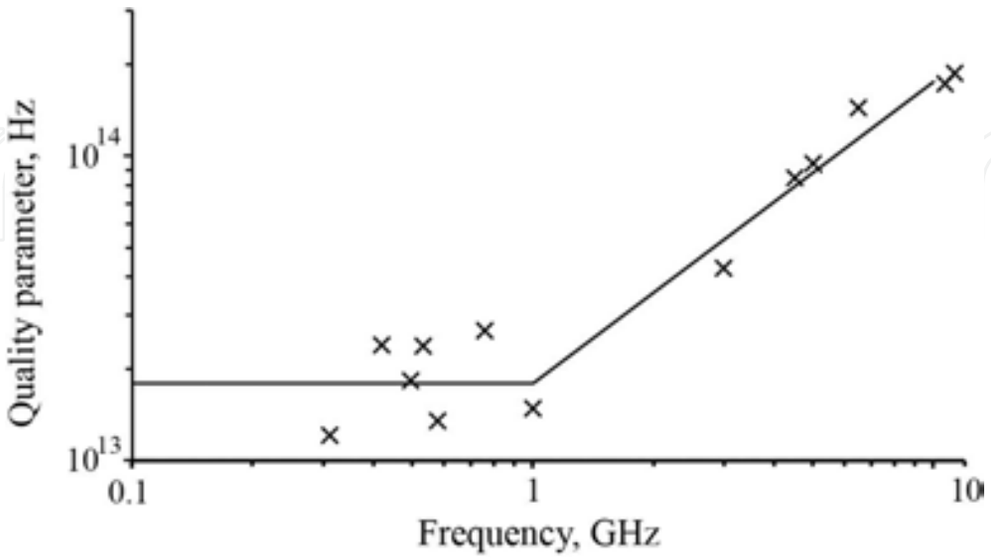

Figure 20. Quality parameter's frequency dependence for diamond-based PLSs.

f, GHz	Diamond	YAG	Sapphire	$LiNbO_3$	
	Our data, [10]	[25]	[26]	[27]	[28]
1	0.9	0.2 ~ 0.3	0.2	0.3*	0.4
2	1.8	1.0*	0.8*	1.0*	1.5
4.5	4	5.2*	4.1*	5.1*	8.0
8	7.1	16.0*	12.8*	15.8*	

*Calculated in the Akhiezer approximation.

Table 3. Microwave acoustic attenuation (dB/cm) in diamond in comparison with other crystals at room temperature.

4. Modeling of microwave acoustic properties of "Me1/AlN/Me2/diamond" piezoelectric layered structure

4.1. Equivalent circuit and frequency dependences of equivalent parameters for «Me1/AlN/Me2/diamond» PLS

HBAR's equivalent parameters are close concerned with specified equivalent scheme of device and are important in view of HBAR modeling and application, for example, the AFC calculation, matching of devices, etc. PLS equivalent scheme introduced in Ref. [6] is represented in **Figure 21**.

$$\begin{aligned} C_0 &\approx -\frac{1}{\omega_n \mathrm{Im} Z_{11}}, \\ R_n &= \max \mathrm{Re} Z_e\left(f_{p,n}\right), \\ k_n^2 &= \frac{R_n C_0 \omega_{p,n}}{Q_n}, \\ C_n &= \frac{C_0}{k_n^2}, \\ L_n &= \frac{k_n^2}{\omega_{p,n}^2 C_0} = \frac{1}{\omega_{p,n}^2 C_n}. \end{aligned} \tag{36}$$

Here C_0 and C_n are static and dynamic capacities, R_n is loss of resistance, k_n is the electromechanical coupling coefficient, L_n is dynamic inductance, $\omega_{p,n} = 2\pi f_{p,n}$ is angular frequency of parallel resonance.

Frequency dependence of equivalent parameters for the 1a, 1b, and 1c resonators (PLS #3) is represented in **Figure 22**. As one can see, there is a complex frequency dependence of equivalent parameters which requires an accurate choice of operational frequency bands.

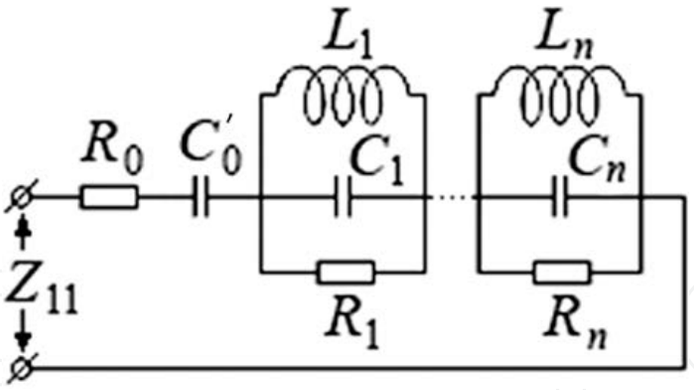

Figure 21. PLS equivalent scheme.

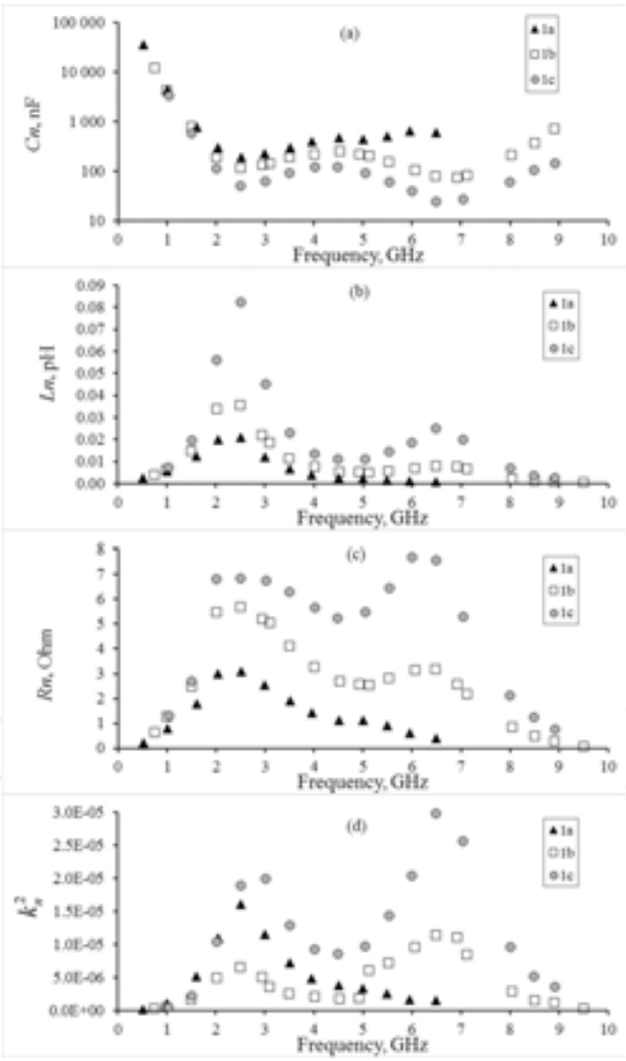

Figure 22. Frequency dependence of equivalent parameters for the 1a, 1b, and 1c resonators (PLS #3, see **Figure 7** and Section 3.1).

4.2. Peculiarities of PLS acoustic wave excitation by thin film piezoelectric transducer

Both Q and $Q \times f$ measured for a lot of PLSs have nonmonotonic frequency dependence with a number of local maximums and minimums. Such complex dependence can be explained in terms of form-factor m, which was introduced in Ref. [29] for the TFPT conjugated with the acoustic line. It was shown in Ref. [29] that the frequency dependence of the acoustic power W radiated by the TFPT into the substrate can be considered by the relation: $W \sim |m|^2$. In Ref. [21], it was shown that such approach is also valid for the "Me1/piezoelectric/Me2/substrate" PLS. A simple analytic expression of the form-factor m for PLS without top electrode [21,29] can be written as

$$m = \frac{\cos\phi_p \cos\phi_M - \frac{Z_P}{Z_M}\sin\phi_P \sin\phi_M + i\left(\frac{Z_M}{Z_P}\cos\phi_p \sin\phi_M + \frac{Z_P}{Z}\sin\phi_P \cos\phi_M\right)}{\sin^2\frac{\phi_P}{2}}. \quad (37)$$

Here Z_P, Z_M, and Z are the acoustic impedances of the piezoelectric film, inner metal electrode, and substrate, respectively; $\varphi_M = k_M d_M$ and $\varphi_P = k_P d_P$ are the phase shifts inserted by the metal film and piezoelectric layer; k_M and k_P are the wave vectors in those layers; d_M and d_P are thicknesses of these layers. However, Eq. (37) should be considerably modified in order to take into account the top electrode. Unfortunately, such equation could not be written in a compact form, but the proper matrix system of equations was represented in Ref. [21].

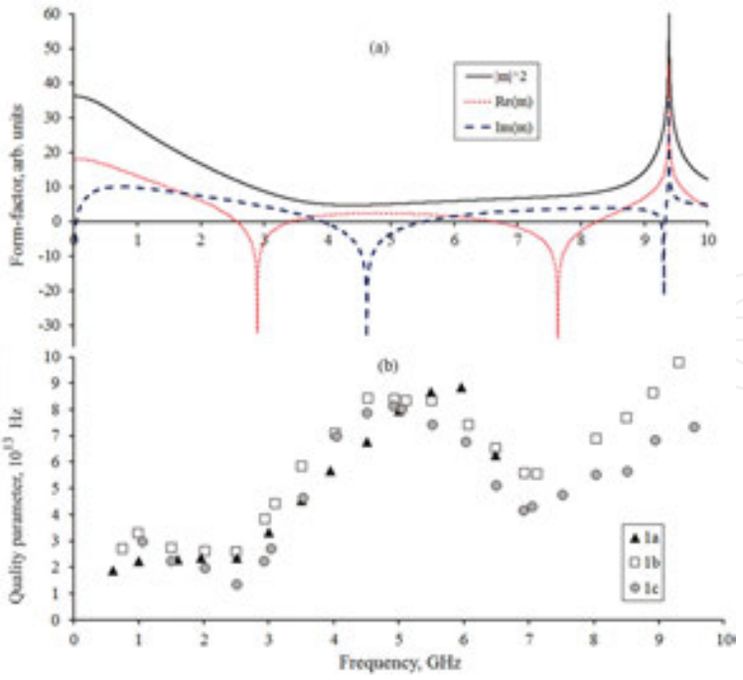

Figure 23. Frequency dependence of form-factor $|m|^2$, Re(m), and Im(m): (a) calculated data, and (b) comparison with experimentally obtained $Q \times f$ product for the PLS #3 (see **Figure 7** and Section 3.1).

It is easy to show that as a rule the minimums of $|m|^2$ should be associated with maximum-radiated acoustic power, while maximums of form-factor should result in low W or even the absence of an acoustic signal. A number of form-factor calculations were done by our special computer software. As one can see from **Figure 23**, there is a strong correlation between the frequency dependences of Q ($Q \times f$) and $|m|^2 = f(\omega)$, as well as with the Re(m) and Im(m) functions. It can be easily seen that frequency bands with high Q ($Q \times f$) should be associated with minimal values of the Im(m), low Q ($Q \times f$) values correlate with minimal Re(m), and low TFPT effectiveness coincides with maximal $|m|^2$. Note that Re(m) minimums arise at frequency bands concerned with the ~ $p(\lambda_{AlN}/4)$ resonances of AlN film (p is the odd integer). So the acoustoelectronic device will be more efficient at such operating frequencies where the flat regions with minimal values of the $|m|^2$ function are realized. As a result, such preliminary computer analysis makes possible defining the proper operating frequencies before constructing a device.

4.3. 2D FEM simulation results of acoustic wave propagation in diamond-based PLS

The 2D FEM simulations were carried out with the use of Comsol Multiphysics Simulation Software. Material data on the density, elastic constants, acoustic attenuation, etc. for all the layers and diamond substrate were taken from Refs. [16, 21, 30]. Such PLS parameters and acoustic processes as distribution of elastic displacement fields within all the parts of PLS (cross-sections of substrate and TFPT), AFR modeling, calculation of the wavelengths and phase velocities of acoustic modes of different types, identification of its types, etc. have been studied in detail. Symmetrical boundary conditions on the lateral borders of diamond substrate were used in order to satisfy the condition of zero normal displacement components as $(\vec{n}, \vec{U})=0$, where $\vec{n}$ is a unit vector of the normal to the lateral border, and $\vec{U}$ is a unit vector of the wave elastic displacement. Visualization of elastic displacement fields gave us an instrument of analysis of acoustic wave excitation because all the waves propagating in lateral directions should be reflected under the condition $w = m(\lambda/2)$, where w is a substrate width, λ is a wavelength, and m is an integer. In this 2D case, as a result of wave reflection, a lot of enabled acoustic waves such as symmetrical (S_n) and antisymmetrical (A_n) Lamb waves of different orders, and Rayleigh waves could be observed in a given frequency band. Overtones of longitudinal BAW, which were of great importance in a practical sense have been investigated in a wide frequency band in order to establish the energy-trapping effect in diamond-based PLS. Calculated layered structure was chosen as to be close to the experimentally studied one as PLS #3. Widths of top Al electrode, AlN layer, and Mo bottom electrode were equal to 400 μm, while diamond's widths were taken as 1000 or 1100 μm. Thicknesses of Al, AlN, Mo layers, and diamond substrate were equal to 164 nm, 624 nm, 169 nm, and 392 μm, respectively. During the calculation by the "Eigenfrequency" option, a lot of sequentially excited acoustic resonant modes have been observed, and the main attention was paid on the patterns of mechanical displacements, which were associated with one or the other type of acoustic wave. Because the most waves in PLS have a dispersion of phase velocities, it was important to study its frequency dependences. The form of more convenient presentation of calculated results was the YX cross-section of a sample (**Figure 24**). Wave propagation can be observed along

http://dx.doi.org/10.5772/62630

the X-axis (Rayleigh and Lamb waves) or along the Y-axis (mainly longitudinal acoustic waves).

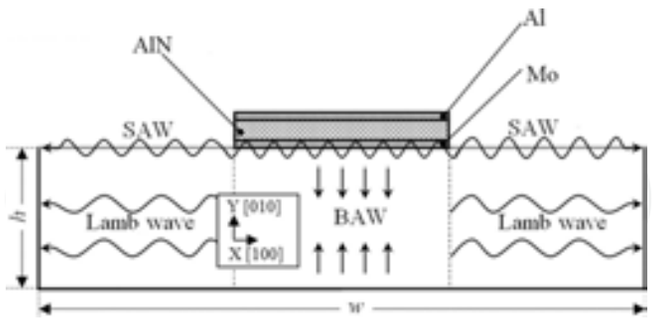

Figure 24. Typical scheme of diamond-based PLS.

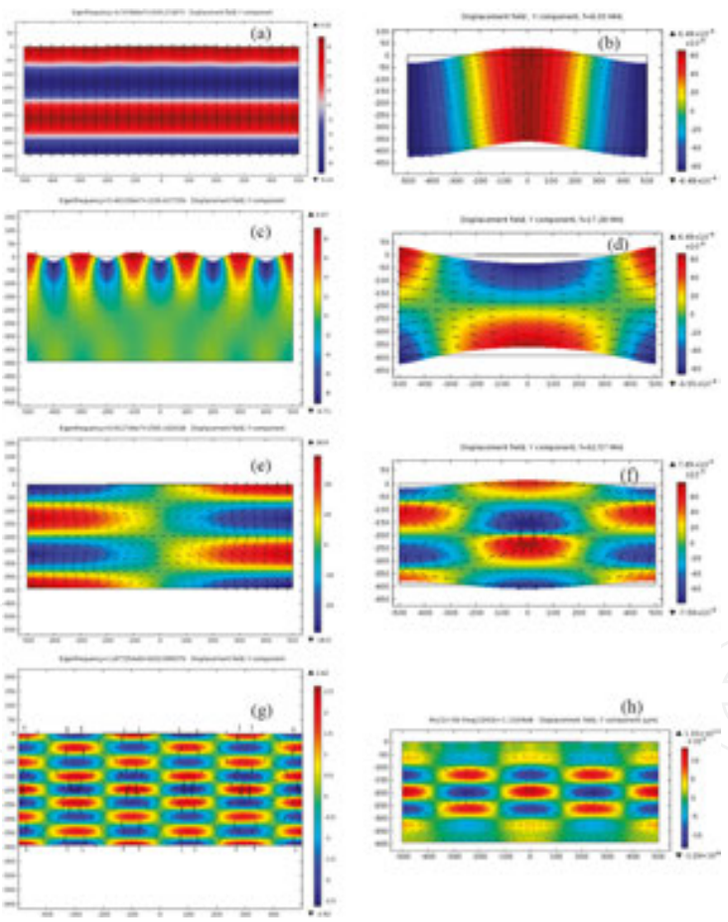

Figure 25. Displacement fields of some modes obtained by 2D FEM simulation for diamond-based PLS #3: (a) third overtone of the *L* mode at ~67 MHz; (b) the A_0 mode at resonant frequency ~8.03 MHz; (c) the *R* mode at resonant frequency ~54.6 MHz; (d) the S_0 mode at resonant frequency ~17.28 MHz; (e) the S_{2l} Lamb mode near the critical frequency (f_{cr} = 68.86 MHz); (f) the S_{2t} Lamb mode near the critical frequency (f_{cr} = 63.84MHz); (g) the A_{4l} Lamb mode; and (h) A_{4t} Lamb mode. Red color is associated with Y-component of elastic displacement in vertical direction up, and blue color defines such value in vertical direction down. Elastic displacements are presented in a magnified scale.

In **Figure 25**, the patterns of elastic displacements for some acoustic waves are presented. One can clearly see the arrangement of displacement vectors designated by arrows. Color graphics serves, knowing the displacement along the Y-direction (up or down) and its magnitude. For example, if we take into account Rayleigh wave displacements (**Figure 25c**), there are ten $\lambda_R/2$, which are placed along the width of the diamond substrate (1000 μm); so, $\lambda_R = 200$ μm at 54.613 MHz. As a result, the phase velocity of Rayleigh wave propagating on the diamond surface is equal to 10922.6 m/s. In a similar manner, the phase velocities for all observed eigenmodes have been calculated.

Effect of energy trapping was observed in the conventional piezoelectric resonators and was explained by authors [31] as a total internal reflection of acoustic beam on the vertical borders within the resonator's aperture. Such effect was observed in HBARs too [32], but it has a more complex nature. As an example, the appearance of energy trapping in the PLS #3 is represented in **Figure 26**. It should be noted that realization of energy trapping is strongly concerned with the BAW wavelength, lateral dimensions, substrate thickness, and TFPT aperture. In the case of PLS #3, the energy trapping regime in the steady state was established, beginning the 12th BAW overtone at frequencies above ~268 MHz.

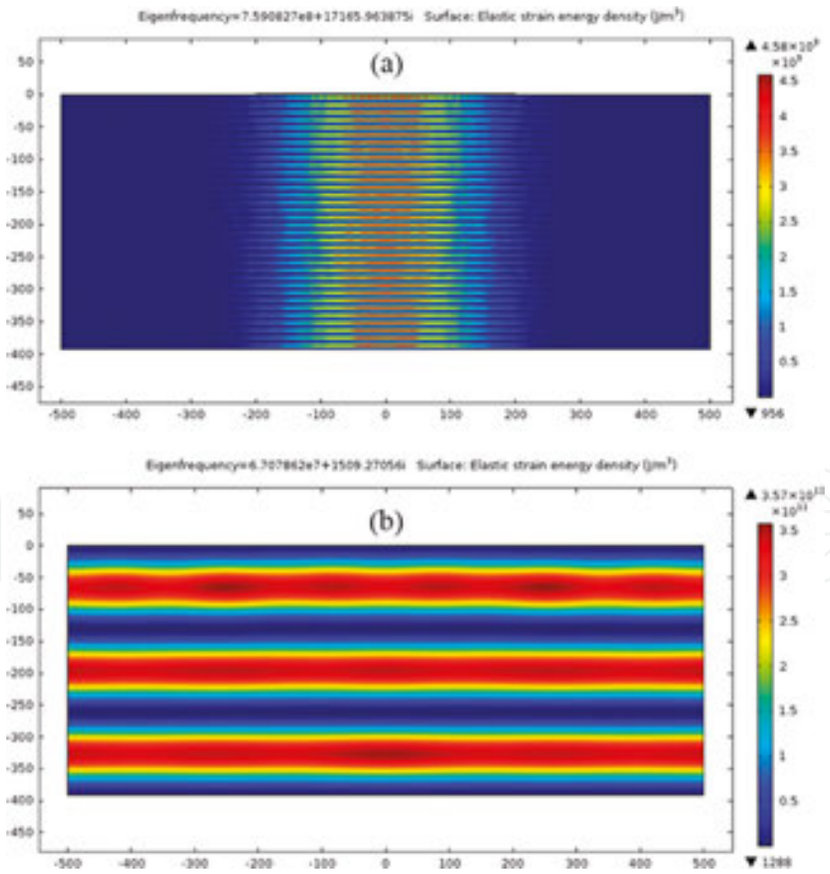

Figure 26. Energy trapping in the PLS #3: (a) energy trapping realized for 34th BAW overtone (~759 MHz); (b) absence of energy trapping on 3rd overtone (~67 MHz).

4.4. Identification, selection and classification of acoustic waves of different types

PLS has a sophisticated acoustic spectrum. Generally speaking there are three normal bulk acoustic waves propagating along any crystalline direction within a substrate: Rayleigh waves on free top and bottom substrate surfaces; symmetrical and antisymmetrical Lamb plate waves when the thickness of substrate is comparable to the wavelength. Presence of piezoelectric layer gives a possibility of excitation not only to bulk waves in vertical direction, but also to modified dispersive Rayleigh waves, including Sezawa wave with highest phase velocity, and Love waves, belonging to the *SH*-wave class. Excitation Rayleigh or *SH* waves separately will be defined as an occurrence of appropriate piezoelectric constants at the given configuration of electrodes and orientation of piezoelectric film (see Section 2.3). Mass loading of TFPT results in "softening" of the mutual region "substrate + TFPT" and gives a useful possibility of energy trapping for longitudinal BAW in the vertical direction, so that the BAW energy is localized within the TFPT aperture under certain conditions. Note that within TFPT region, the SAW phase velocity will have a smaller value than the same at the free diamond surface. Fine interferometric effects could be observed as a consequence of acoustic wave reflection from lateral borders of the substrate or TFTP.

Type and order of the acoustic modes were defined, taking into account the directions of elastic displacement vectors, location, and the number of homogeneous areas of elastic displacements along vertical and horizontal axes when the fields of elastic displacements analogous to **Figure 25** have been analyzed.

Dispersive Lamb waves are of special interest because there are a lot of types and orders of dispersive branches for its phase velocities. In order to distinguish Lamb modes, let us remember that the critical wavelengths (or critical frequencies) for each Lamb mode should be defined [33] as

$$\left.\begin{array}{l} h = \dfrac{\lambda_l}{2}, \dfrac{3\lambda_l}{2}, \dfrac{5\lambda_l}{2}, \ldots \\ h = \lambda_t, 2\lambda_t, 3\lambda_t, \ldots \end{array}\right\} \text{for } S_n \text{ waves,}$$
$$\left.\begin{array}{l} h = \lambda_l, 2\lambda_l, 3\lambda_l, \ldots \\ h = \dfrac{\lambda_t}{2}, \dfrac{3\lambda_t}{2}, \dfrac{5\lambda_t}{2}, \ldots \end{array}\right\} \text{for } A_n \text{ waves,} \tag{38}$$

where h is the plate thickness, λ_l and λ_t are the wavelengths of longitudinal and transverse (shear) bulk acoustic waves, respectively. Note that at critical frequency, each Lamb mode will degenerate into a standing wave whose phase velocity will tend to infinity and elastic displacement field will correspond to either a longitudinal or transverse type. So, at the frequencies below a critical one, a given Lamb mode should not exist. Using Eq. (38), one can calculate the critical frequencies for each Lamb wave excited in a plate and define the point of creation of such mode. Note that PLS critical frequencies could weakly differ from the ones for pure plate. Now, the necessity for distinguishing between Lamb modes of the same type and order has been recognized. It would be a good thing to highlight this fact as a mode

creation's point, and as a result, here and after, the lower index "*l*" or "*t*" will be used to designate not only critical frequencies, but also the dispersive curves calculated for such specified Lamb modes. Usually, such differences had not been taken into account, and, in our opinion, some mistakes of classification of the Lamb mode spectrum were previously made.

4.5. Phase velocity dispersion curves and critical frequencies for acoustic waveguide Lamb modes

Dispersive properties of Lamb waves are important in a physical and practical sense. Based on 2D FEM simulation of PLS #3, all the possible modes have been observed within the 0–250 MHz band, than the mode's identification and classification have been executed [34]. As a result, the dispersion curves for the phase velocities for a lot of Lamb modes have been obtained (**Figure 27**). As one can see, the phase velocities of the A_0 and S_0 modes converge to the phase velocity of Rayleigh wave at high frequency. It is suitable to say that such A_0 and S_0 modes have a broad application in acoustic nondestructive control devices, sensors, etc. Note that the conditions of Rayleigh wave excitation are fulfilled at both the substrate surfaces, but the effective phase velocity on the top surface should be lower due to the TFPT loading.

Phase velocities of all other A_n and S_n ($n \geq 1$) modes have a high dispersion, and at high frequency finally converge to the phase velocity of shear BAW propagating along the [010] direction of the diamond. Super-high magnitudes of phase velocities of Lamb waves near the creation points have no physical meaning and can be treated as standing longitudinal/transverse modes.

Analyzing a set of dispersive curves, one can notice that the difference between Lamb modes with respect to a mode creation's point (e.g., A_{nl} vs A_{nt}, or S_{nl} vs S_{nt}, etc.) has an important meaning, and such features are necessary for detailed explanation of Lamb wave spectrum in a wide sense.

Taking into account Eq. (38), one can see that critical frequencies for S_{nl} and A_{nl} plate modes ($n \geq 1$) coincide with the resonant frequencies of odd and even overtones of longitudinal bulk acoustic wave, respectively. For example, such relations should be fulfilled as $f_{cr}(S_{1l}) = f_r(L_1)$, $f_{cr}(S_{2l}) = f_r(L_3)$, …, $f_{cr}(A_{1l}) = f_r(L_2)$, $f_{cr}(A_{2l}) = f_r(L_4)$, etc. As a result, this fact can also be used for Lamb mode identifying. But it should be noted that real critical frequencies for Lamb waves propagated in PLS studied differ slightly from that predicted by Eq. (38) due to the influence of mass loading as well as phase shifts arising as a consequence of deposition of thin-film layers on the top of substrate.

In the similar manner the dispersive curves of phase velocities of Lamb waves can be obtained at other frequency bands and will be useful for preliminary analysis of design of advanced acoustoelectronics devices.

http://dx.doi.org/10.5772/62630

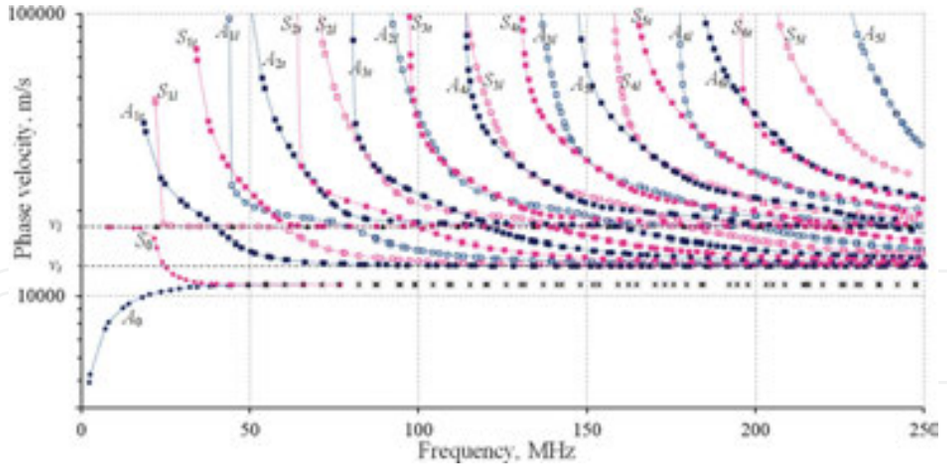

Figure 27. Frequency dependences of phase velocity for diamond-based piezoelectric layered structure PLS #3.

5. Conclusion

A lot of "Al/AlN/Mo/(100) diamond" PLSs have been studied both theoretically and experimentally within a wide frequency band of 0.5–10 GHz. At first time, the highest among known material quality parameter $Q \times f \sim 10^{14}$ Hz for the IIa-type synthetic diamond at operational frequency ~10 GHz has been found. Analyzing the elastic displacement fields of PLS obtained by 2D FEM simulation, the Lamb modes as well as other types of elastic waves have been identified. Dispersive curves for phase velocities of all the acoustic waves observed have been plotted for the studied PLSs in the frequency range 0–250 MHz, and it is easy to expand such approach up to a higher frequency band. It has been established that 2D FEM visualization of the elastic displacement fields gives a fine possibility to an accurate study of the fundamental properties of elastic waves of different types. Analyzing the obtained data, one should note that the modified classification of Lamb modes in regard with its creation point as a longitudinal or transverse standing wave at critical frequency should be additionally introduced. Results on UHF acoustic attenuation of IIa-type synthetic single crystalline diamond have been presented and discussed in terms of Akhiezer and Landau–Rumer mechanisms of phonon–phonon interaction. It was found that the frequency of transformation of Akhiezer's mechanism into Landau–Rumer's was estimated as ~1 GHz in the IIa-type synthetic diamond at room temperature. As a result, single crystalline diamond will be a promising substrate for acoustoelectronic devices when operating frequency should be higher than the units of GHz, because the UHF acoustic attenuation in diamond in comparison with other commonly used crystals will be considerably lower.

Acknowledgements

This study was performed by a grant of Russian Science Foundation (project #16-12-10293).

Author details

Boris P. Sorokin[1,2*], Gennady M. Kvashnin[1], Arsenii V. Telichko[1,2], Sergey I. Burkov[3] and Vladimir D. Blank[1,2]

*Address all correspondence to: bpsorokin2@rambler.ru

1 Technological Institute for Superhard and Novel Carbon Materials, Moscow, Troitsk, Russian Federation

2 Moscow Institute of Physics and Technology, Dolgoprudny, Russian Federation

3 Siberian Federal University, Krasnoyarsk, Russian Federation

References

[1] Lakin K.M., Kline G.R., McCarron K.T. High-Q microwave acoustic resonators and filters. IEEE Transactions on Microwave Theory and Techniques. 1993;41(12):2139–2146. DOI: 10.1109/22.260698

[2] Mirea T., DeMiguel-Ramos M., Clement M., Olivares J., Iborra E., Yantchev V., et al. AlN solidly mounted resonators for high temperature applications. In: Proceedings of the Ultrasonics Symposium (IUS), 2014 IEEE International; 3–6 September; Chicago, IL. IEEE; 2014. p. 1524-1527. DOI: 10.1109/ULTSYM.2014.0377

[3] Sorokin B.P., Kvashnin G.M., Volkov A.P., Bormashov V.S., Aksenenkov V.V., Kuznetsov M.S., et al. AlN/single crystalline diamond piezoelectric structure as a high overtone bulk acoustic resonator. Applied Physics Letters. 2013;102(11):113507. DOI: 10.1063/1.4798333

[4] Zhang H., Pang W., Yu H., Kim E.S. High-tone bulk acoustic resonators on sapphire, crystal quartz, fused silica, and silicon substrates. Journal of Applied Physics. 2006;99(12):124911. DOI: 10.1063/1.2209029

[5] Baumgartel L., Kim E.S. Experimental optimization of electrodes for high Q, high frequency HBAR. In: Proceedings of the Ultrasonics Symposium (IUS), 2009 IEEE International; 20–23 September; Rome. IEEE; 2009. p. 2107–2110. DOI: 10.1109/ULTSYM.2009.5441814

[6] Mansfeld G.D., Alekseev S.G., Polzikova N.I. Unique properties of HBAR characteristics. In: Proceedings of the Ultrasonics Symposium, 2008 (IUS'2008). IEEE; 2–5 November; Beijing. IEEE; 2008. p. 439–442. DOI: 10.1109/ULTSYM.2008.0107

[7] Sorokin B.P., Kvashnin G.M., Kuznetsov M.S., Burkov S.I., Telichko A.V. Influence of the temperature and uniaxial pressure on the elastic properties of synthetic diamond

single crystal. In: Proceedings of the Ultrasonics Symposium (IUS), 2012 IEEE International; 7–10 October; Dresden. IEEE; 2012. p. 763–766. DOI: 10.1109/ULTSYM.2012.0190

[8] Anthony T.R., Banholzer W.F., Fleischer J.F., Wei L., Kuo P.K., Thomas R.L., et al. Thermal diffusivity of isotopically enriched ^{12}C diamond. Physical Review B. 1990;42(2):1104–1111. DOI: 10.1103/PhysRevB.42.1104

[9] Wells G.M., Palmer S., Cerrina F., Purdes A., Gnade B. Radiation stability of SiC and diamond membranes as potential x-ray lithography mask carriers. Journal of Vacuum Science & Technology B. 1990;8(6):1575–1578. DOI: 10.1116/1.585118

[10] Sorokin B.P., Telichko A.V., Kvashnin G.M., Bormashov V.S., Blank V.D. Study of microwave acoustic attenuation in a multifrequency bulk acoustic wave resonator based on a synthetic diamond single crystal. Acoustical Physics. 2015;61(6):669–680. DOI: 10.1134/S1063771015050164

[11] Aleksandrov K.S., Sorokin B.P., Burkov S.I. Effective piezoelectric crystals for acoustoelectronic, piezotechnics and sensors. Novosibirsk: SB RAS; 2007. pp. 501.

[12] Burkov S.I., Zolotova O.P., Sorokin B.P., Aleksandrov K.S. Effect of external electrical field on characteristics of a Lamb wave in a piezoelectric plate. Acoustical Physics. 2010;56(5):644–650. DOI: 10.1134/S1063771010050088

[13] Burkov S.I., Zolotova O.P., Sorokin B.P. Calculation of the dispersive characteristics of acoustic waves in piezoelectric layered structures under the effect of DC electric field. IEEE Transactions on Ultrasonics, Ferroelectrics, and Frequency Control. 2012;59(10): 2331–2337. DOI: 10.1109/TUFFC.2012.2458

[14] Kessenich G.G., Lyubimov V.N., Shuvalov L.A. On surface Lamb waves in piezoelectric crystals. Crystallography Reports. 1982;28(3):437–443.

[15] McSkimin H.J., Andreatch P.Jr., Glynn P. The elastic stiffness moduli of diamond. Journal of Applied Physics. 1972;43(3):985–987. DOI: 10.1063/1.1661318

[16] Sotnikov A.V., Schmidt H., Weihnacht M., Smirnova E.P., Chemekova T.Yu., Makarov Y.N. Elastic and piezoelectric properties of AlN and $LiAlO_2$ single crystals. IEEE Transactions on Ultrasonics, Ferroelectrics, and Frequency Control. 2010;57(4):808–811. DOI: 10.1109/TUFFC.2010.1485

[17] Wu S., Ro R., Lin Z.-H., Lee M.-S. Rayleigh surface acoustic wave modes of interdigital transducer/(100) AlN/(111) diamond. Journal of Applied Physics. 2008;104(6):064919. DOI: 10.1063/1.2986215

[18] Wu S., Ro R., Lin Z.-X., Lee M.-S. High velocity shear horizontal surface acoustic wave modes of interdigital transducer/(100) AlN/(111) diamond. Applied Physics Letters. 2009;94(9):092903. DOI: 10.1063/1.3093528

[19] Sorokin B.P., Kvashnin G.M., Bormashov V.S., Volkov A.P., Telichko A.V., Gordeev G.I., et al. The manufacturing technology of the UHF transducers based on AlN film

deposited on a synthetic diamond single crystal substrate. Izvestiya Vysshikh Uchebnykh Zavedeniy Seriya "Khimiya I Khimicheskaya Tekhnologiya". 2014;57(4):17–21.

[20] Mansfeld G., Alekseev S., Kotelyansky I. Bulk acoustic wave attenuation in langatate. In: Proceedings of the 2001 IEEE International Frequency Control Symposium and PDA Exhibition; 06–08 June; Seattle, WA. IEEE; 2001. p. 268–271. DOI: 10.1109/FREQ.2001.956201

[21] Sorokin B.P., Kvashnin G.M., Telichko A.V., Gordeev G.I., Burkov S.I., Blank V.D. Study of high-overtone bulk acoustic resonators based on the Me1/AlN/Me2/(100) diamond piezoelectric layered structure. Acoustical Physics. 2015;61(4):422–433. DOI: 10.1134/S106377101503015X

[22] Akhiezer A. On acoustic attenuation in solids. Journal of Experimental and Theoretical Physics. 1938;8(12):1318–1329.

[23] Landau L., Rumer Yu. Absorption of sound in solids. Physikalische Zeitschrift der Sowjetunion. 1937;11(18):227–233.

[24] Tabrizian R., Rais-Zadeh M., Ayazi F. Effect of phonon interactions on limiting the f.Q product of micromechanical resonators. In: Proceedings of the Solid-State Sensors, Actuators and Microsystems Conference, 2009. Transducers 2009. International; 21–25 June; Denver, CO. IEEE; 2009. p. 2131–2134. DOI: 10.1109/SENSOR.2009.5285627

[25] Auld B.A. Acoustic fields and waves in solids, Vol. 1. New York, NY: Wiley; 1973. pp. 423.

[26] Fitzgerald T.M., Silverman B.D. Temperature dependence of the ultrasonic attenuation in Al_2O_3. Physics Letters A. 1967;25(3):245–247. DOI: 10.1016/0375-9601(67)90883-3

[27] Mitsui T.V., Abe R., Furuhata Y., Gesi K., Ikeda T., Kawabe K., et al. Landolt-Börnstein, Zahlenwerte und Funktionen aus Naturwissenschaft und Technik. Neue Serie, Gruppe III: Kristall-und Festkörperphysik. Band 3: Ferro- und Antiferroelektrische Substanzen. Berlin-Heidelberg-New York: Springer-Verlag; 1969. pp. 584.

[28] Wen C.P., Mayo R.F. Acoustic attenuation of a single-domain lithium niobate crystal at microwave frequencies. Applied Physics Letters. 1966;9(4):135–136. DOI: 10.1063/1.1754679

[29] Dieulesaint E., Royer D. Elastic waves in solids: applications to signal processing. New York, NY: Wiley; 1980. pp. 511.

[30] Mansfeld G.D., Alekseev S.G., Kotelyansky I.M. Acoustic HBAR spectroscopy of metal (W, Ti, Mo, Al) thin films. In: Proceedings of the Ultrasonics Symposium, 2001 IEEE (Vol. 1); 07–10 October; Atlanta, GA. IEEE; 2001. p. 415–418. DOI: 10.1109/ULTSYM.2001.991652

[31] Shockley W., Curran D.R, Koneval D.J. Trapped-energy modes in quartz filter crystals. The Journal of the Acoustical Society of America. 1967;41(4B):981–993. DOI: 10.1121/1.1910453

[32] Kvashnin G., Sorokin B., Telichko A. Resonant transformation of acoustic waves observed for the diamond based HBAR. In: Proceedings of the Frequency Control Symposium & the European Frequency and Time Forum (FCS), 2015 Joint Conference of the IEEE International; 12–16 April; Denver, CO. IEEE; 2015. p. 396–401. DOI: 10.1109/FCS.2015.7138866

[33] Viktorov I.A. Rayleigh and Lamb waves: physical theory and applications. 1st ed. Springer, New York; 1967. pp. 154. DOI: 10.1007/978-1-4899-5681-1

[34] Sorokin B.P., Kvashnin G.M., Telichko A.V., Novoselov A.S., Burkov S.I. Lamb waves dispersion curves for diamond based piezoelectric layered structure. Applied Physics Letters. 2016;108: 113501.

IntechOpen